npj | climate and atmospheric science

Article

Published in partnership with CECCR at King Abdulaziz University

https://doi.org/10.1038/s41612-024-00642-0

Late Pleistocene island weathering and precipitation in the Western Pacific Warm Pool

Check for updates

Zhaojie Yu[1,2,3] ✉, Jiaoyang Ruan[4,5] ✉, Lina Song[1], Kyung-Sook Yun[4,5], Xiaojie Tang[1], Christophe Colin[6], David J. Wilson[7], Haowen Dang[8], Pedro N. DiNezio[9], Fengming Chang[1], Xiaolei Pang[10], Franck Bassinot[11] & Shiming Wan[1]

Deciphering past climate variability in the Western Pacific Warm Pool (WPWP), the Earth's largest heat and moisture centre, is vital for understanding the global climate system. Nevertheless, its long-term evolution remains controversial, largely due to ambiguities in existing proxy interpretations and discrepancies between records. Here, we present a weathering and erosion reconstruction from the WPWP spanning the last 140,000 years, based on the mineralogy and geochemistry of a sediment core from offshore of northern New Guinea. The paleo-weathering reconstruction is consistent with the simulated precipitation evolution on nearby islands, thereby suggesting a close coupling between climate variability and island weathering in a tropical setting. In addition, our combined data-model interpretation of WPWP climate history shows many similarities to the East Asian Summer Monsoon (EASM) variability over orbital timescales. Overall, our study highlights the critical role of precession-paced interhemispheric energy redistribution, via the West Pacific meridional sea-surface pressure gradient, in linking orbital-scale WPWP climate and EASM variability.

Heat content and convection in the Western Pacific Warm Pool (WPWP) play a significant role in modulating the global energy and moisture balance through their links to two key atmospheric circulation systems: the zonal Walker circulation and the meridional Hadley circulation[1–3]. As such, the climate dynamics in this region affect the agricultural livelihood of billions of people by controlling precipitation across a large area of Asia and beyond. Indeed, increased rainfall over Southeast Asia and drying over the west coast of the U.S.A. during 1981–2018 is attributed to the deep convection changes associated with an almost two-fold expansion of the annual mean WPWP area compared to the last century[4]. However, given the short timespan of instrumental records, it is critical to understand the WPWP convection and precipitation history over longer timescales using paleoclimate records[3].

Precipitation variability and associated deep convection changes in the WPWP have been inferred for the geological past using proxy records from speleothems[5–10], leaf wax geochemistry[11–14], foraminiferal oxygen isotopes[15–17], and XRF-scan elemental ratios[18–21]. Nevertheless, a coherent spatio-temporal picture of past changes over orbital timescales is yet to emerge because of the complexity of the controlling factors and differences between individual records[22–24]. Although both paleo-proxy and paleo-modelling studies of the tropical monsoon systems[25,26], the El Niño-Southern Oscillation (ENSO)-like system, and the Intertropical Convergence Zone indicate precession-paced variations in deep convection and precipitation[19,27–29], their exact responses to insolation changes differ. These differences could point to spatial variability in the tropical hydroclimate response to insolation forcing[25,30], but might also reflect uncertainties in proxy interpretation[31–33], pointing to the need for additional indicators.

Here, we present a 140,000-year island weathering and erosion reconstruction from the WPWP, based on geochemical and mineralogical analyses in a sediment core from offshore of northern New Guinea (Fig. 1). In the present day, heavy rainfall in the study area is directly linked to

[1]Key Laboratory of Ocean Observation and Forecasting, Institute of Oceanology, Chinese Academy of Sciences, Qingdao 266071, China. [2]Laboratory for Marine Geology, Qingdao Marine Science and Technology Center, Qingdao 266237, China. [3]Center for Ocean Mega-Science, Chinese Academy of Sciences, Qingdao 266071, China. [4]Center for Climate Physics, Institute for Basic Science, Busan, South Korea. [5]Pusan National University, Busan, South Korea. [6]Université Paris-Saclay, CNRS GEOPS, 91405 Orsay, France. [7]Institute of Earth and Planetary Sciences, University College London and Birkbeck, University of London, Gower Street, London WC1E 6BT, UK. [8]State Key Laboratory of Marine Geology, Tongji University, Shanghai, China. [9]Department of Atmospheric and Oceanic Sciences, University of Colorado Boulder, Boulder, USA. [10]Institute of Ocean Research, Peking University, Beijing, China. [11]LSCE/IPSL, CEA-CNRS-UVSQ, Université Paris-Saclay, F-91191 Gif-sur-Yvette, France. ✉e-mail: yuzhaojie@qdio.ac.cn; jiaoyangruan@pusan.ac.kr

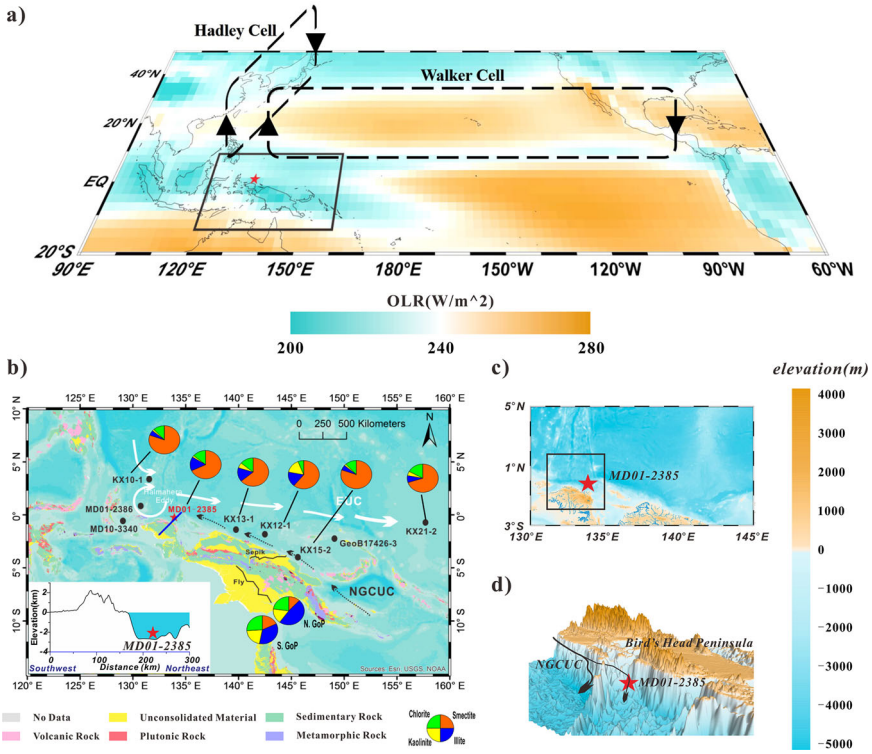

Fig. 1 | Geological and oceanographic setting. **a** Map of regional outgoing longwave radiation (OLR), showing intense convection over the Indo-Pacific region (green shading) linked to the circulation of the Walker and Hadley cells (shown schematically). The mean OLR data are from 1991 to 2020: https://psl.noaa.gov/data/gridded/data.olrcdr.interp.html. The black box indicates the map area for panel (b), and the red star indicates the location of core MD01-2385. **b** Lithological map showing core locations and clay mineral data (where available) for cores MD01-2385 (this study), MD10-3340[84], MD01-2386[71], GeoB17426-3[27], KX cores[39], and cores from the northern and southern Gulf of Papua (GoP)[85,86]. Black dotted arrows = New Guinea Coastal Undercurrent (NGCUC), white arrows = Equatorial Undercurrent (EUC), and white circle = Halmahera Eddy. Inset panel shows the topography along the southwest to northeast transect marked by the blue line. Sources for the lithological data: https://www.noaa.gov/organisation/information-technology/noaa-geoplatform and the elevation data: https://www.ncei.noaa.gov/maps/grid-extract/. **c** Map of small mountain rivers that supply sediments to core MD01-2385. The black box represents the area of the precipitation simulation data (1.855°N-1.855°S, 131.25°–135°E). **d** Seafloor bathymetry near core MD01-2385.

convective activity, for which the regional Outgoing Longwave Radiation is an effective proxy[34], under the influence of two atmosphere-ocean circulation modes: the Walker and Hadley circulations (Fig. 1a). Based on monthly rainfall data, three climatic regions can be identified in the Indo-Pacific region (Supplementary Information and Fig. S1). Major and trace element geochemistry and clay mineralogy were measured in the fine detrital fraction (<2 μm) at a high temporal resolution in marine sediments from core MD01-2385 (0.22°S, 134.24°E, water depth 2602 m; Fig. 1). Major elements and clay mineralogy data were published recently[24] for the upper 12.70 m of the core, spanning 0–40 ka BP, and are here expanded to 140 ka BP (please see Fig. S2 for its age model), accompanied by new trace element data[35]. To further explore the climatic factors controlling the past weathering intensity, and the mechanisms behind the WPWP climate variability, we also present the results from a Community Earth System Model (CESM) simulation, which captures Pleistocene orbital-scale climate oscillations in good agreement with paleo-precipitation and temperature reconstructions from various proxies from around the globe[36–38].

Results and discussion

Reconstructing island weathering variability in the Western Pacific Warm Pool

Our recent late glacial and Holocene study suggested that the terrigenous sediment input to core MD01-2385 was mostly derived directly from local sources in northwest New Guinea via small mountainous rivers[24] (Fig. 1c). This inference is also supported by similarities in the clay mineral assemblage (Fig. 1b), rare earth element (REE) patterns and ratios (Fig. S3a, b), and Zr/Cr versus Sc/Ni ratios (Fig. S3c) between core MD01-2385 and nearby core MD10-3340 from the northern margin of New Guinea island. Clays carried from further upstream by the New Guinea Coastal Under Current (NGCUC) and the New Guinea Coastal Current (NGCC) (Fig. 1b) may also have provided a sediment source and need to be treated as an alternative hypothesis. Nevertheless, the high sedimentation rate of core MD01-2385 (~18 cm/kyr) suggest such oceanic contribution plausibly smaller than the influx from rivers. In addition, the fairly consistent provenance through time (Fig. S3) and the lack of correlation between geochemical provenance indicators and weathering proxies in core MD01-2385 (Fig. S4) excludes a significant effect on those weathering and erosion proxies from sediment source changes. There is also no clear ~100-kyr cycle in the clay compositions or in other weathering or erosion indicators in the core (Figs. S5, S6). The absence of such cyclicity appears to rule out a major influence from sea-level changes on ~100-kyr timescales[39]. Finally, we note that the weathering of the underlying volcano below the ice cap does not represent a significant sediment source for our core, considering the transport distance and the complicated blocking of the topography (Fig. 1d).

The chemical index of alteration (CIA) indicates the extent of removal of soluble base cations (Ca, Na, K) relative to aluminium (Al) from a given bedrock, with higher values indicating a higher degree of chemical weathering (i.e. higher chemical weathering relative to total denudation, where denudation is the sum of chemical weathering and physical erosion). For core MD01-2385, the CIA in the clay-sized fraction ranges from 74 to 78, with generally higher values during the glacial marine isotope stages (MIS) 2, 4, and 6, and during cold substages within the interglacial MIS 5 (MIS 5b and 5d)[24] (Fig. 2c). These values are generally lower than clay-fraction CIA values from the nearby islands of Luzon, Borneo, and Sumatra, as well as the Fly river clay fraction, which range from 80 to 95[40–42]. Both the absolute values and orbital-scale pattern may initially appear surprising, because (i) northwest New Guinea experiences a warm and humid climate, which could be expected to lead to intense weathering and a high degree of chemical weathering similar to those nearby areas[40,41], and (ii) chemical weathering intensity could be expected to decrease strongly when temperature decreases on orbital timescales[43].

We propose that these apparent discrepancies arise because the weathering processes in northwest New Guinea are strongly controlled by the physical erosion induced by heavy rainfall, in combination with the small mountainous rivers and the lack of floodplains. In such a highly erosional regime, increases in precipitation can be expected to enhance physical erosion rates and decrease soil residence times and sediment storage times in the drainage basins, leading to less time for sediments to be fully chemically weathered, hence driving the delivery of detrital minerals characterised by a lower degree of chemical weathering (i.e. lower CIA). In other words, while physical erosion rates and chemical weathering fluxes would both be enhanced under wet conditions, the chemical weathering

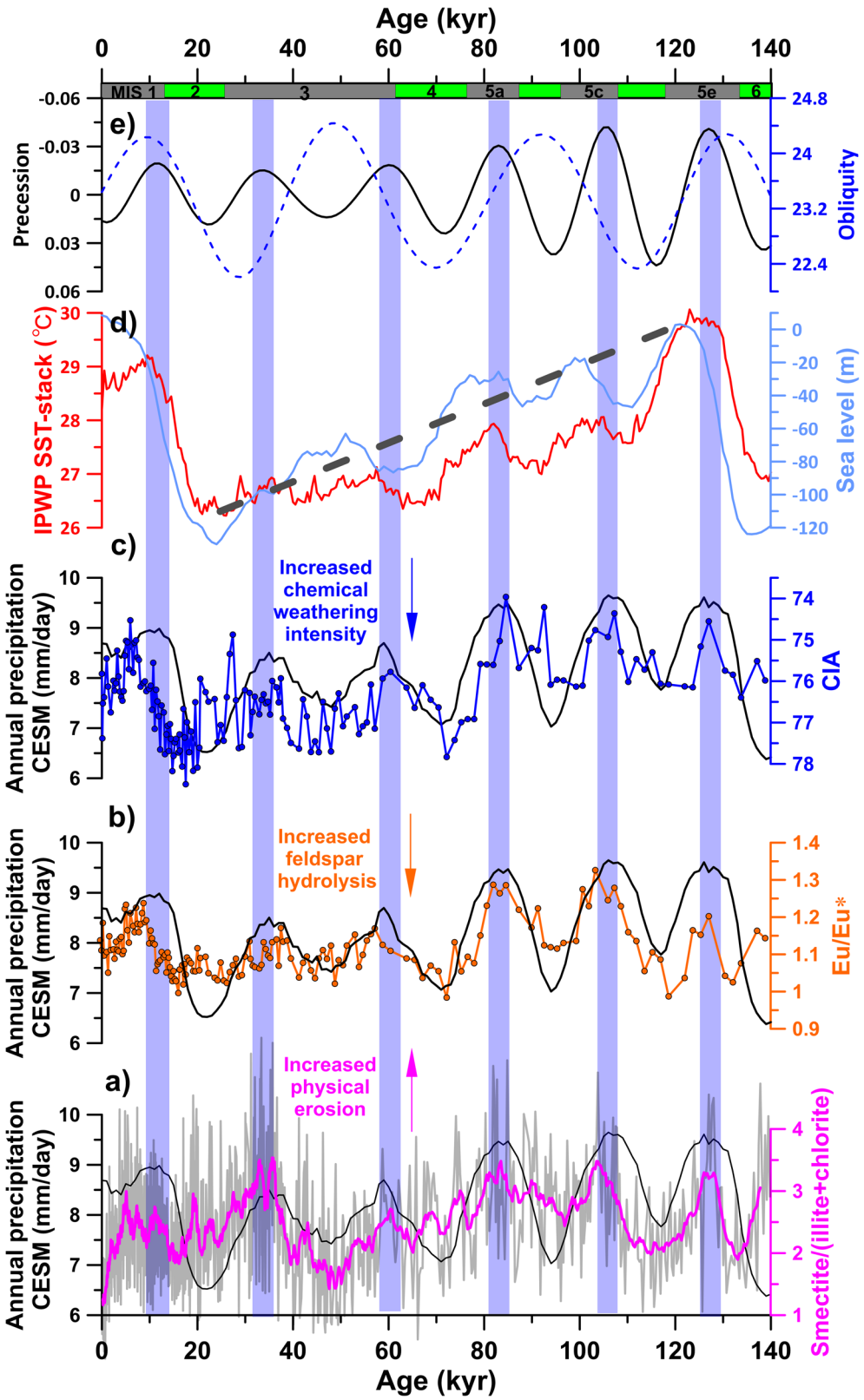

Fig. 2 | Orbital-scale trends of climate, weathering, and erosion in the tropical Western Pacific since 140 ka. a Smectite/(illite+chlorite) ratios as a physical erosion indicator (this study; the curve shows a 13-point average of the original data). **b** Chemical weathering in core MD01-2385 (this study) inferred from Eu/Eu* = 2 Eu/(Sm+Gd), where the element data are UCC-normalised[87]. **c** Chemical weathering in core MD01-2385 (this study) based on the chemical index of alteration (CIA), calculated from CIA = $[Al_2O_3/(Al_2O_3+CaO^*+Na_2O+K_2O)] \times 100$, where CaO* represents CaO associated with the silicate fraction[88]. Note the inverse scale for CIA. In (**a**–**c**), the simulated annual precipitation in the inferred source region for core MD01-2385 is also shown for comparison (black lines). **d** Stacked sea surface temperature (SST) from the Indo-Pacific Warm Pool (IPWP)[29], and global sea level based on a global stack[89]. The dark grey dashed line denotes the general decline in sea level during the last glacial cycle. **e** Orbital parameters of precession (black solid line; inverse scale) and obliquity (blue dashed line)[66]. Precessional cycles are indicated, with light blue bars representing precession minima.

fluxes would increase by proportionally less than the erosion rates, such that the degree of weathering of those sediments would decrease[43]. As a corollary, we argue that drier conditions, on orbital timescales, would lead to weaker runoff and reduced physical erosion rates, but a higher degree of chemical weathering of the detrital sediments due to their longer residence times in soils. The above observations are in line with our millennial timescale finding that low physical denudation rates and high chemical weathering intensities are coincident with North Atlantic millennial-scale cool climate events[24]. Note that this weathering phenomenon has been shown to be characteristic of high-relief drainage basins lacking major alluvial plains, such as Taiwan island[44], and differs from systems with large alluvial plains and longer sediment residence times, where increased precipitation in the catchment leads to a higher degree of chemical weathering[45,46].

A higher weathering degree during glacial and cold substage periods can also be inferred from the new europium anomaly (Eu/Eu*) data in core MD01-2385. The Eu/Eu* values range from 0.98 to 1.33 and are anti-correlated with the CIA, with lower Eu/Eu* values (i.e. smaller positive Eu anomalies) during the orbital-scale periods of MIS 2, 4, 5b, 5d, and 6 (Fig. 2b). Such anomalies are unlikely to have been driven by provenance changes, such as those related to arc evolution or dissection, as the observed changes occur cyclically and over short (orbital) timescales. It is also unlikely that this phenomenon was caused by redox-driven changes in the properties of the seawater, as the Eu concentration in the detrital clay sediment is several orders of magnitude higher than in seawater-derived phases[47]. New Guinea and the surrounding islands mainly comprise basic to intermediate volcanic rocks and their derived sediments (Fig. 1b). Such rocks are rich in olivine, pyroxene, and plagioclase[48], and are characterised by positive Eu anomalies[49]. The Eu is mainly contained in plagioclase, which is more resistant to chemical weathering than olivine and pyroxene[50]. Therefore, an increased chemical weathering intensity could possibly lead to enhanced plagioclase hydrolysis, which would release Eu to the weathering fluid, thereby generating a positive Eu anomaly in the fluid and a negative (or weaker positive) Eu anomaly (i.e. lower Eu/Eu* value) in the detrital residue[49,50]. The latter signal in the clay fraction would be transported via river sediments to the ocean and recorded in core MD01-2385. Notably, positive Eu anomalies have been observed in the seawater of the West Pacific marginal seas and were attributed to a signature of dissolved basaltic inputs[51], which supports the importance of basalt weathering as a driver of geochemical signatures in this region. The less positive Eu anomalies measured in the detrital sediment appear to represent the counterpart to that dissolved signal.

The clay assemblage of core MD01-2385 consists predominantly of smectite (22–88%, average 67%), while illite (4–49%, average 17%), chlorite (5–28%, average 14%), and kaolinite (0.5–9%, average 2%) are less abundant (Fig. S5). The clay minerals in this region are mainly related to detrital input from New Guinea, rather than to authigenic processes[24,52]. Although distant sediments carried by ocean currents may also be important sources of clay, we expect their contribution to be smaller than the direct input from local rivers, given the high sedimentation rate in core MD01-2385. Temporal variations in smectite content are inverse to the illite and chlorite content, such that smectite/(illite+chlorite) ratios can be used to represent mineralogical variations of the clay-size fraction (Fig. S5 and Fig. 2a). Illite and chlorite are thought to be mostly products of the strong mechanical denudation of metamorphic and other crystalline basement rocks under physical weathering regimes[53]. In contrast, smectite and kaolinite are produced by intense chemical weathering in warm tropical or subtropical climates, under conditions of either high rainfall (kaolinite) or moderate rainfall (smectite)[53]. Hence, the high smectite content in core MD01-2385 is consistent with relatively intense weathering and the abundance of basaltic rocks in the river basins of New Guinea island[24]. Since the smectite/(illite +chlorite) ratios were lower during MIS 2, 4, 5b, 5d, and 6 (Fig. 2a), it appears that smectite production and/or transport decreased during the periods with locally dry conditions, and increased during wet intervals. Therefore, we propose that the supply of smectite to the core site may have been mainly controlled by strong physical erosion of the widely-distributed volcanic rocks during wet intervals, leading to an enhanced smectite content relative to background sedimentation of illite and chlorite. This scenario does not imply that chemical weathering cannot affect smectite/(illite +chlorite) ratios, but rather emphasises the importance of physical denudation relative to chemical weathering in the supply of smectite in this setting. In this view, the smectite/(illite+chlorite) ratios could be interpreted as an indicator for the physical erosion of soils developed on basaltic rocks of New Guinea island. This conclusion is consistent with, and adds further support to, the findings of previous studies[24,39,52].

Chemical weathering of tropical basaltic islands covering only ~1% of the global land area is estimated to account for ~10% of the total global CO_2 consumed by silicate weathering and could therefore play an important role in the global carbon cycle[54–56]. Additionally, the weathering of basaltic islands favours the production of smectite, which is iron-rich and has a loose porous structure that facilitates the adsorption of organic particles[40,52]. The inputs of smectite from basalt weathering would not only transport soluble iron to the WPWP and thereby enhance marine productivity, but could help in transporting and burying terrestrial organic carbon particles[39]. Both factors would facilitate a transfer of CO_2 from the atmosphere to the ocean and/or ocean sediments, and would cause at least a transient storage of carbon, even if some of the organic carbon is ultimately released back to the atmosphere by oxidation[54,55]. The combination of the erosion-dominated weathering regime that we infer for New Guinea and the rapid response of weathering and erosion indicators to climate variability in this region supports the potential importance of the above processes operating in these regions for the carbon cycle. By enhancing carbon storage, the accelerated erosion and smectite supply during warmer and wetter periods could potentially promote negative feedbacks in the climate system, but further quantitative studies would be required to assess the timescales over which such feedbacks could play out and their impact at a global scale.

Spatial patterns of orbital precipitation changes in the Indo-Pacific region

The above three proxy records of weathering and erosion in core MD01-2385 are expected to be controlled by precipitation and/or temperature in the sediment source regions of the New Guinea islands. Reconstructions of regional sea surface temperature (SST) and global sea-level for the last glacial cycle both indicate clear glacial-interglacial cyclicity[1,29] (Fig. 2d), in contrast to our precession-dominated weathering records (Fig. 2a–c). Such a difference is clearly exemplified during MIS 5, in which the weathering and erosion records show peaks of approximately equal magnitude for MIS 5a, 5c, and 5e, whereas the SST and sea-level curves show relatively lower peaks for MIS 5a and 5c compared to MIS 5e (Fig. 2a–d). Therefore, neither temperature changes nor sea-level changes appear to have been the main drivers of the weathering and erosion changes. Hence, we consider that our physical erosion and chemical weathering indicators in core MD01-2385 are mainly driven by variability in precipitation induced by convective intensity in the central WPWP.

To test our climatic interpretation and to further investigate the central WPWP history, we present a continuous 140,000-year precipitation time series simulated with the CESM version 1.2 (see Methods). Annual mean precipitation was extracted from the simulation for Northwest New Guinea (1.855°N-1.855°S, 131.25°-135°E, Fig. 1c), encompassing the core MD01-2385 site and its plausible sediment source on nearby islands. The simulated precipitation record shows excellent agreement with the paleo-precipitation variability inferred from the MD01-2385 weathering and erosion reconstructions, with precipitation peaks repeatedly occurring at precession minima and precipitation lows at precession maxima (Fig. 2a–c).

However, the precipitation intensity reconstructed by both our proxies and modelling clearly differ from other Indo-Pacific reconstructions, including Borneo stalagmite $\delta^{18}O$ records[6,7,9,10] and riverine runoff inferred from the XRF-scanning ln(Ti/Ca) proxy in cores MD05-2920[19] and MD06-3067[57] (Fig. 3). This comparison likely points to a marked spatial heterogeneity in rainfall responses in this tropical region.

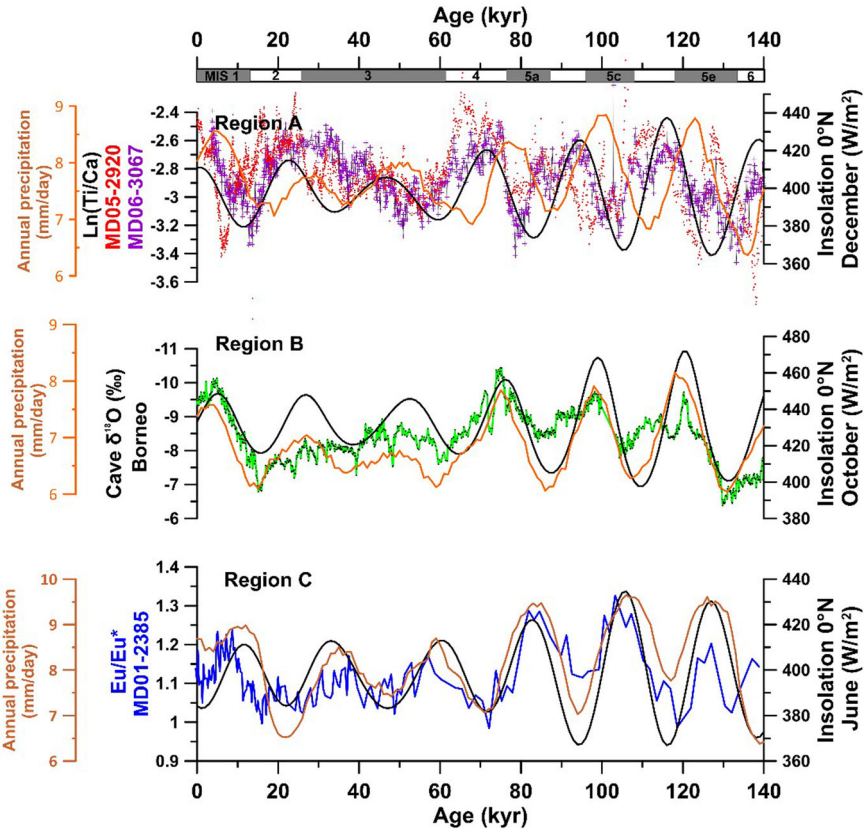

Fig. 3 | Orbital-scale heterogeneity in rainfall patterns in the Indo-Pacific region. The distribution of hydrological regions A to C is shown in the Supplementary Information and Fig. S1. Region A: ln(Ti/Ca) in MD05-2920[19] (red) and MD06-3067[57] (purple), with rainfall consistent with December insolation at 0°N. Region B (green): Borneo stalagmite $\delta^{18}O$ record[6,7,10], with rainfall consistent with October insolation at 0°N. Region C (blue): Eu/Eu* ratio in MD01-2385 (this study), with rainfall consistent with June insolation at 0°N. Note that the axis direction for all proxy records is such that upwards indicates inferred higher rainfall. The precipitation simulation results from near the three regional proxy records are also compared accordingly. The region of precipitation extraction is a model grid square of dimensions 3.75° × 3.75°, which contains the core locations and potential sediment provenance sources (see Fig. S1 for detailed locations).

Surprisingly, the spatial heterogeneity of these orbital-scale precipitation records is fairly consistent with the modern hydroclimate. The ln(Ti/Ca) records are located in region A and their orbital variations are in phase with December insolation at 0°N[19,57] (Fig. 3), consistent with the modern maximum precipitation occurring during the boreal winter (Fig. S1). The Borneo stalagmite $\delta^{18}O$ record is from region B, which in the modern climate has biannual rainfall peaks (October–November and March–May; Fig. S1) associated with two crossings of the Intertropical Convergence Zone[58]. The orbital variability in the Borneo stalagmite record is in-phase with October insolation at 0°N[7,9,10] (Fig. 3), which is consistent with the largest of those two modern peaks in October-November (Fig. S1). In contrast, the weathering records in core MD01-2385 are synchronous with June insolation at 0°N (Fig. 3), which is consistent with the modern location of western New Guinea island in region C, which experiences maximum precipitation in June-July (Fig. S1). Most of region C is likely to be influenced by the westwards flow of the Indonesian Throughflow, which not only transfers warm water from the WPWP during boreal summer, but also brings the convective centre generated by these warm waters to the region, thus increasing precipitation[58]. Conversely, during boreal winter, the relatively cold waters suppress precipitation[58].

Combining the CESM simulation, we found that the simulated precipitation corresponds well with the proxy records from the regions B and C, yet with phase differences of a few kyrs between the simulation and the proxies in the region A (Fig. 3). This observation may be due that the region A is geographically located in the Northern Hemisphere (Fig. S1), but regional climate may also be affected by signals from the Southern Hemisphere, with complex regional land-sea distributions and intense air-sea interactions[24,29]. Nevertheless, both proxy data and models highlight the spatial heterogeneity in the orbital scale climate evolution in the WPWP.

This conclusion is consistent with an independent study which also indicated spatially heterogeneous glacial-interglacial changes in hydroclimate over the Indo-Pacific[59]. Influence on the hydroclimate from the exposure of continental shelves seems to be restricted to the Maritime Continent and fairly minor in the open Western Pacific[60], suggested by the distinct differences between the weathering records from core MD01-2385 and the temporal pattern of sea-level variability (Fig. S6).

Western Pacific Warm Pool climate linked to the East Asian Summer Monsoon

A recent study used planktonic foraminifera from multiple deep-sea cores to reconstruct the oxygen isotope composition of surface seawater ($\delta^{18}O_{sw}$) and the ocean heat content in the Indo-Pacific Warm Pool (IPWP) (Fig. 4d)[29]. The $\delta^{18}O_{sw}$ and ocean heat content stacks are consistent with each other, and both changed synchronously with Chinese stalagmite $\delta^{18}O$ records (a proxy for the East Asia Summer Monsoon; EASM) in the precession band (Fig. 4e). Specifically, an increase in the ocean heat content in the IPWP corresponds to heavier $\delta^{18}O$ values in seawater and lighter $\delta^{18}O$ values in stalagmites[29] (Fig. 4d, e). Therefore, those authors proposed that an increased ocean heat content in the warm pool leads to enhanced evaporation at the tropical sea surface and transfer of the water vapour to the neighbouring land areas, thereby increasing monsoon rainfall in East Asia. As such, that study indicated that changes in heat content in the warm pool could regulate the water vapour transport between the Pacific Ocean and the Asian continent over orbital timescales[29].

The precipitation history in the central WPWP, as inferred here using three weathering proxies in core MD01-2385 and a transient CESM simulation, displays similar long-term trends and orbital cyclicity to the stacked $\delta^{18}O_{sw}$ and ocean heat content records from the IPWP[29] and to the Chinese stalagmite $\delta^{18}O$ records[5] (Fig. 4). More specifically, all of these records show strong co-variation in their dominant precession band[5] (Fig. 4 and Supplementary Fig. S6), although the precession periods for the weathering indicators do not show perfect precession bands of 23-kyr. This phenomenon is not unique to our records, but is widely identified in previous sediment-derived weathering records, such as haematite/goethite (29-kyr) and kaolinite/illite ratios (28-kyr, 25-kyr, and 22-kyr) in ODP Site 1143[61], K_2O/Al_2O_3 ratio (20-kyr) in core MD12-3432[62], smectite/(illite +

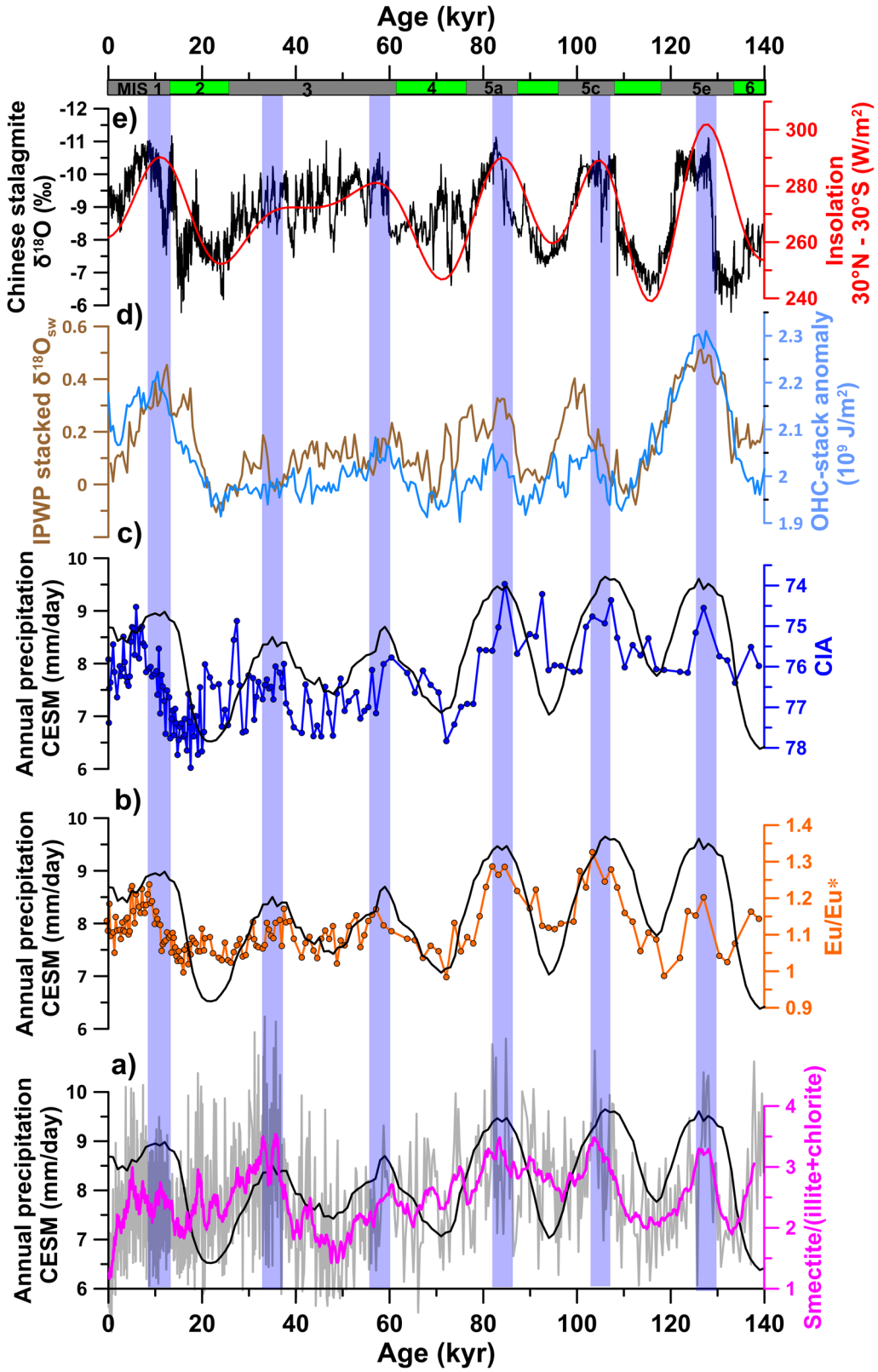

Fig. 4 | Precession-dominated hydrological changes in the low to mid-latitudes of Eastern Asia. a, **b**, and **c** are the same as in Fig. 2. **d** Stacked surface seawater oxygen isotope ($\delta^{18}O_{sw}$) and stacked ocean heat content (OHC) anomaly, both from the Indo-Pacific Warm Pool (IPWP)[29]. **e** Stalagmite $\delta^{18}O$ records from Sanbao Cave as an indicator of the East Asian Summer Monsoon[5], and insolation gradient from 30 °N to 30 °S in June[66]. Precessional cycles are indicated, with light blue bars representing precession minima.

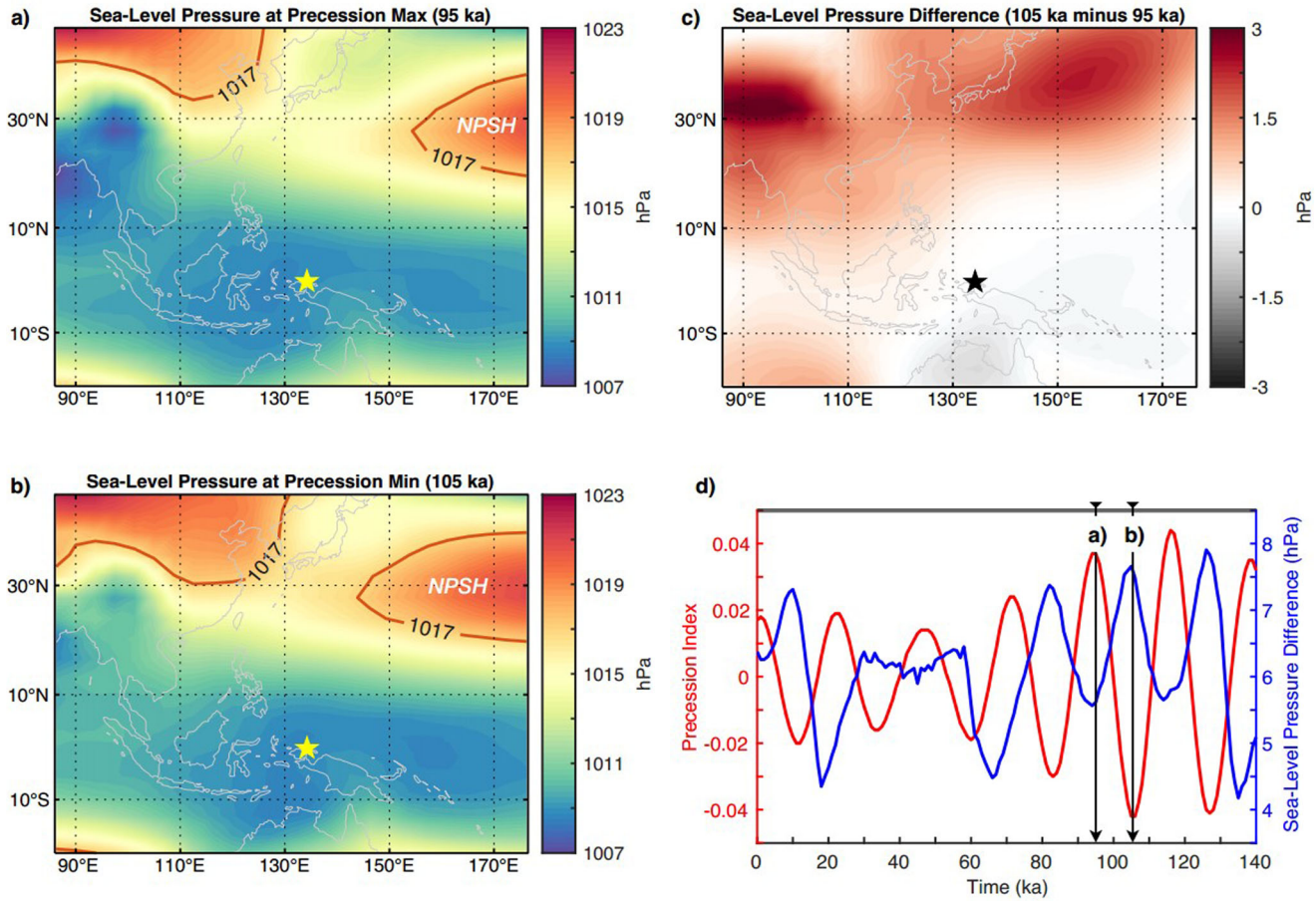

Fig. 5 | Simulated regional sea-level pressures at different phases of the precession cycle. a–c Sea-level pressure at 95 ka (precession maximum), 105 ka (precession minimum), and their difference (105 ka–95 ka). **d** Temporal evolution of the orbital precession index (orange line) and the sea-level pressure difference between 30°N and 10°S at ~150°E as an indicator for the Hadley circulation (blue line), with black arrows indicating the time slices in (**a**, **b**). Red line in (**a**, **b**) represents the sea-level pressure contour of 1017 hPa, and the location of the North Pacific Subtropical High (NPSH) is also marked. Note that the western boundary of the NPSH in (**b**) is shifted westwards by ~10° of longitude compared to (**a**). Yellow and black stars indicate the location of core MD01-2385.

chlorite) ratios in core MD77-171 (21-kyr)[63], and kaolinite/quartz ratios in core MD77-169 (17-kyr)[64], etc. We also filter the precession-band signal from these records (Fig. S7) and find that their correspondence is generally good within the age-model tuning age error (2–5 kyr). However, in a few intervals, we also find some phase differences, such as the three periodic peaks since 70 ka in the smectite/(illite+chlorite) ratios, and the two peaks of MIS 5c and 5e in the Eu/Eu* and CIA records. To further explore this issue, we carry out segmental spectral analysis of the 0–70 ka and 70–140 ka intervals of the weathering records and find that the precession cycle from 70 to 140 ka is closer to 23-kyr than that during 0–70 ka. This finding may reflect the greater amplitude of precession cycles during 70–140 ka (mainly MIS 5) than during 0–70 ka, making the precessional response clearer to resolve in geological records that will naturally contain some additional noise (Fig. S8). Despite the complexities, these results support a close hydrologic linkage between the tropical Pacific Ocean and the Asian continent in the precession band[29].

Furthermore, we explored the dynamic mechanism linking the WPWP climate and the EASM rainfall by analysing regional precipitation and sea-surface pressures in the western Pacific Ocean during the past 140,000 years (Fig. 5 and S9). The simulated precipitation differences between the precession maximum and minimum (Fig. S9c) showed a "Sandwich" spatial distribution, supported by our proxy data compilation (Fig. 3), and similar to what we observe in modern-day instrument data (Fig. S1a). The precession-paced interhemispheric energy redistribution (Fig. 4e) modulates the convective intensity in the WPWP (Fig. 4a–d), which could in turn influence the EASM rainfall (Fig. 4e) through its coupling to the Hadley circulation and the North Pacific Subtropical High (NPSH)[3,5,19,65]. This mechanism seems to be consistent with dominant in-phase variations in the weathering proxies in core MD01-2385 and the low-latitude interhemispheric insolation gradient at precession bands[66] (Fig. S7).

The NPSH and its westward extension influence the EASM rainfall by regulating the regional winds and associated moisture transport[67]. As part of the descending branch of the meridional Hadley cell circulation, the NPSH is closely coupled with the ascending motion and associated convective activity in the WPWP[3,68]. We find that, during precession minima (or interhemispheric insolation gradient maxima), strong convection in the WPWP enhances the Hadley cell circulation (Fig. 5b, d). This scenario not only leads to a precipitation and weathering increase in the WPWP (as demonstrated by our proxy data and model simulation in Figs. 2–4 and Fig. S9) and a negative sea-surface pressure anomaly (Fig. 5c), but it boosts the northward transmission of heat and moisture, which eventually strengthens and expands the NPSH westwards towards the East China Sea (Fig. 5b). This enhanced and westward-shifted NPSH facilitates moisture transport into East Asia through the near-surface circulation, leading to increased EASM precipitation in southern China[5] (Fig. 4e). Conversely, during precession maxima (or interhemispheric insolation gradient minima), the shallower WPWP convection would reduce the precipitation and island weathering in the WPWP and would weaken the Hadley cell (Fig. 5a, d and Fig. S9), as well as driving eastward shrinking of the NPSH[3]. In summary, our analyses emphasise the importance of the tropical interhemispheric insolation gradient in modulating the Hadley cell circulation intensity and therefore the NPSH variability. Our combined reconstruction and simulation results

support a low-latitude driven hypothesis, as recently highlighted with cosmogenic ^{10}Be fluxes from Chinese loess at orbital scales[65], and radiocarbon and sedimentological proxies from the Gulf of Alaska at millennial scales[69], and further indicate its possible driving forces from the warming pool.

Methods

Sediment core, regional setting, and age model

Core MD01-2385 (0.22°S, 134.24°E, water depth 2602 m) was collected from north of Bird's Head Peninsula, offshore of northwest New Guinea in the tropical Western Pacific during the R/V Marion Dufresne IMAGES VII Cruise in 2001 (Fig. 1). The lithology consists of light brown nannofossil ooze, occasionally interbedded with silty clay.

The island of New Guinea is characterised by small mountainous river catchments with very high physical erosion rates (1.5×10^3 t/km^2/yr) and sediment discharge (1.7×10^9 t/yr), reflecting its active tectonics, basalt-dominated rocks, and a tropical climate with heavy rainfall and high runoff[48]. Furthermore, the steep relief, small watershed areas, narrow shelf off northeastern New Guinea, and short transport distances lead to efficient sediment transfer to the oceans[39,48]. In such a source-to-sink regime, weathering and erosion processes can respond rapidly to changes in precipitation, and therefore weathering and erosion proxies have the potential to be used as independent precipitation indicators[24,39].

The age model for core MD01-2385 from 0 to 40 ka has been published previously[24,70]. It is based on 10 accelerator mass spectrometry (AMS) ^{14}C dates on well-preserved mixed planktonic foraminifera G. ruber and G. sacculifer in the size fraction > 150 μm[70] (Fig. S2). The age model for >40 ka was established by tuning the planktonic foraminifera G. ruber δ^{18}O record of core MD01-2385 to the stacked G. ruber δ^{18}O record from nearby cores GeoB17426-3[27] and MD01-2386[71] (Fig. S2). The age models for both those cores were previously established by correlating their benthic foraminifera C. wuellerstorfi δ^{18}O records to the LR04 benthic δ^{18}O stack[72]. Based on this chronology, the 32.4 m-long core MD01-2385 provides a continuous record from 0 to 140 ka, with an average linear sedimentation rate of 18 cm/kyr (ranging from 11 to 54 cm/kyr) (Fig. S2).

Mineralogical and geochemical analysis

Clay mineralogy was analysed on a total of 899 samples from core MD01-2385, with an average resolution of ~156 y/sample[24] (Fig. S5). The clay minerals were identified by X-ray diffraction (XRD) using a D8 ADVANCE diffractometer with CuKα radiation in the Laboratory of IOCAS. Oriented mounts of non-calcareous clay-sized (<2 μm) particles were analysed following the method described previously[73,74]. Briefly, deflocculation was accomplished by successive washing with distilled water after removing carbonate and organic matter by treating with acetic acid (25%) and hydrogen peroxide (15%), respectively. The clay mineral particles smaller than 2 μm were separated according to Stokes' law. Three XRD runs were performed, following air-drying, ethylene-glycol solvation for 24 h, and heating at 490 °C for 2 h. The clay minerals were identified according to the position of the (001) series of basal reflections on the three XRD diagrams. The mixed layers composed mainly of smectite-illite (15–17 Å) are included in the "smectite" category. Semi-quantitative estimates of peak areas of the basal reflections for the main clay mineral groups of smectite (15–17 Å), illite (10 Å), and kaolinite/chlorite (7 Å) were carried out on the glycolated curve using the MacDiff software. The relative proportions of kaolinite and chlorite were determined based on the ratio from the 3.57/3.54 Å peak areas. Replicate analyses of a few selected samples indicate a precision of ±2% (2σ). Based on the XRD method, the semi-quantitative evaluation of each clay mineral has an accuracy of ~4%.

Major and trace element concentrations were measured on 182 samples of the detrital clay fraction (<2 μm), after organic matter and carbonate removal. Analyses were conducted by inductively coupled plasma–atomic emission spectrometry (ICP-AES) and ICP mass spectrometry (ICP-MS), following the method described previously[75]. Analytical uncertainties were <1% for major elements and <3% for trace elements (2 SD). Using clay-sized sediments rather than bulk sediments minimises bias from sediment sorting during transport and is therefore more suitable for tracing weathering intensity on the continents, although the clay size fraction can potentially be influenced by sediment recycling[75,76].

Community Earth System Model simulation

We examined the WPWP climate history using a transient climate simulation that was recently conducted using the Community Earth System Model version 1.2 (CESM1.2)[36,37]. The CESM1.2 includes CAM4 atmospheric physics (~3.75° horizontal resolution, 26 vertical levels), the POP2 ocean model (~3° horizonal resolution, 25 depths), CLM4.0 land physics, and CICE4 sea-ice components. This transient simulation was forced by time-varying (updated every 100 years) insolation[77], Northern Hemispheric ice sheets, and greenhouse gases[78,79]. Considering the weaker climatic sensitivity of CESM1.2 compared to paleo-proxy estimates[80,81] and other Earth System Models[82], the CO_2 forcing was scaled by a factor of 1.5 in this simulation. Consistent with other transient climate simulations of different model complexities[80,83], this model applied an orbital acceleration factor of 5 to balance high-demanding computational resources and the proper simulation of ocean circulation dynamics at the timescales of interest.

Data availability

All data are available in the Supplementary Material.

Received: 11 October 2023; Accepted: 10 April 2024;
Published online: 18 April 2024

References

1. Cane, M. A. A role for the tropical Pacific. *Science* **282**, 59–61 (1998).
2. Yun, K.-S., Timmermann, A. & Stuecker, M. F. Synchronized spatial shifts of Hadley and Walker circulations. *Earth Syst. Dyn.* **12**, 121–132 (2021).
3. Chiang, J. C. H. The tropics in Paleoclimate. *Annu. Rev. Earth Planet. Sci.* **37**, 263–297 (2009).
4. Roxy, M. et al. Twofold expansion of the Indo-Pacific warm pool warps the MJO life cycle. *Nature* **575**, 647–651 (2019).
5. Cheng, H. et al. The Asian monsoon over the past 640,000 years and ice age terminations. *Nature* **534**, 640–646 (2016).
6. Partin, J. W., Cobb, K. M., Adkins, J. F., Clark, B. & Fernandez, D. P. Millennial-scale trends in west Pacific warm pool hydrology since the Last Glacial Maximum. *Nature* **449**, 452–455 (2007).
7. Carolin, S. A. et al. Northern Borneo stalagmite records reveal West Pacific hydroclimate across MIS 5 and 6. *Earth Planet. Sci. Lett.* **439**, 182–193 (2016).
8. Ayliffe, L. K. et al. Rapid interhemispheric climate links via the Australasian monsoon during the last deglaciation. *Nat. Commun.* **4**, 1–6 (2013).
9. Meckler, A., Clarkson, M., Cobb, K., Sodemann, H. & Adkins, J. Interglacial hydroclimate in the tropical West Pacific through the Late Pleistocene. *Science* **336**, 1301–1304 (2012).
10. Carolin, S. A. et al. Varied response of western Pacific hydrology to climate forcings over the last glacial period. *Science* **340**, 1564–1566 (2013).
11. Windler, G., Tierney, J. E., Zhu, J. & Poulsen, C. J. Unraveling glacial hydroclimate in the Indo-Pacific Warm Pool: perspectives from water isotopes. *Paleoceanogr. Paleoclimatol.* **35**, e2020PA003985 (2020).
12. Tierney, J. E., Oppo, D. W., Rosenthal, Y., Russell, J. M. & Linsley, B. K. Coordinated hydrological regimes in the Indo-Pacific region during the past two millennia. *Paleoceanography* **25**, PA1102 (2010).
13. Niedermeyer, E. M., Sessions, A. L., Feakins, S. J. & Mohtadi, M. Hydroclimate of the western Indo-Pacific Warm Pool during the past 24,000 years. *Proc. Natl Acad. Sci.* **111**, 9402–9406 (2014).
14. Konecky, B., Russell, J. & Bijaksana, S. Glacial aridity in central Indonesia coeval with intensified monsoon circulation. *Earth Planet. Sci. Lett.* **437**, 15–24 (2016).

15. Gibbons, F. T. et al. Deglacial $\delta^{18}O$ and hydrologic variability in the tropical Pacific and Indian Oceans. *Earth Planet. Sci. Lett.* **387**, 240–251 (2014).
16. Pei, R. et al. Evolution of sea surface hydrology along the western australian margin over the Past 450 kyr. *Paleoceanogr. Paleoclimatol.* **36**, e2021PA004222 (2021).
17. Mohtadi, M. et al. North Atlantic forcing of tropical Indian Ocean climate. *Nature* **509**, 76–80 (2014).
18. Fraser, N. et al. Precipitation variability within the West Pacific Warm Pool over the past 120 ka: evidence from the Davao Gulf, southern Philippines. *Paleoceanography* **29**, 1094–1110 (2014).
19. Tachikawa, K. et al. The precession phase of hydrological variability in the Western Pacific Warm Pool during the past 400 ka. *Quat. Sci. Rev.* **30**, 3716–3727 (2011).
20. Kuhnt, W. et al. Southern Hemisphere control on Australian monsoon variability during the late deglaciation and Holocene. *Nat. Commun.* **6**, 1–7 (2015).
21. Xiong, Z. et al. Rapid precipitation changes in the tropical West Pacific linked to North Atlantic climate forcing during the last deglaciation. *Quat. Sci. Rev.* **197**, 288–306 (2018).
22. Mohtadi, M., Prange, M., Schefuß, E. & Jennerjahn, T. C. Late Holocene slowdown of the Indian Ocean Walker circulation. *Nat. Commun.* **8**, 1–8 (2017).
23. Leduc, G., Vidal, L., Tachikawa, K. & Bard, E. ITCZ rather than ENSO signature for abrupt climate changes across the tropical Pacific? *Quat. Res.* **72**, 123–131 (2009).
24. Yu, Z. et al. Millennial-scale precipitation variability in the Indo-Pacific region over the last 40 kyr. *Geophys. Res. Lett.* e2022GL101646 https://doi.org/10.1029/2022GL101646 (2023).
25. Mohtadi, M., Prange, M. & Steinke, S. Palaeoclimatic insights into forcing and response of monsoon rainfall. *Nature* **533**, 191–199 (2016).
26. Chiang, J. C. H. et al. Role of seasonal transitions and westerly jets in East Asian paleoclimate. *Quat. Sci. Rev.* **108**, 111–129 (2015).
27. Hollstein, M. et al. The impact of astronomical forcing on surface and thermocline variability within the Western Pacific Warm Pool over the past 160 kyr. *Paleoceanogr. Paleoclimatol.* **35**, e2019PA003832 (2020).
28. Clement, A. C & Cane, M. A role for the tropical Pacific coupled ocean-atmosphere system on Milankovitch and millennial timescales. Part I: A modeling study of tropical Pacific variability. (eds & U., Clark & S., Webb & D., Keigwin)*Mechanisms of Global Climate Change at Millennial Time Scales*. 363–371 AGU: Washington, D.C., 1999.
29. Jian, Z. et al. Warm pool ocean heat content regulates ocean–continent moisture transport. *Nature* **612**, 92–99 (2022).
30. Steinke, S. et al. Mid-to late-Holocene Australian–Indonesian summer monsoon variability. *Quat. Sci. Rev.* **93**, 142–154 (2014).
31. Clemens, S. C., Prell, W. L. & Sun, Y. Orbital-scale timing and mechanisms driving Late Pleistocene Indo-Asian summer monsoons: Reinterpreting cave speleothem δ18O. *Paleoceanography* **25**, PA4207 (2010).
32. Parker, S. E. et al. A data–model approach to interpreting speleothem oxygen isotope records from monsoon regions. *Climate* **17**, 1119–1138 (2021).
33. Lachniet, M. S. Climatic and environmental controls on speleothem oxygen-isotope values. *Quat. Sci. Rev.* **28**, 412–432 (2009).
34. Xie, P. & Arkin, P. A. Global monthly precipitation estimates from satellite-observed outgoing longwave radiation. *J. Clim.* **11**, 137–164 (1998).
35. Tang, X. et al. Orbital hydroclimate variability revealed by grain-size evidence in the tropical Pacific Islands since 140 ka. *Glob. Planet. Change*. 104429, https://doi.org/10.1016/j.gloplacha.2024.104429 (2024).
36. Timmermann, A. et al. Climate effects on archaic human habitats and species successions. *Nature* **604**, 495–501 (2022).
37. Yun, K. S. et al. A transient coupled general circulation model (CGCM) simulation of the past 3 million years. *Clim* **19**, 1951–1974 (2023).
38. Ruan, J. et al. Climate shifts orchestrated hominin interbreeding events across Eurasia. *Science* **381**, 699–704 (2023).
39. Dang, H. et al. Orbital and sea-level changes regulate the iron-associated sediment supplies from Papua New Guinea to the equatorial Pacific. *Quat. Sci. Rev.* **239**, 106361 (2020).
40. Liu, Z., Zhao, Y., Colin, C., Siringan, F. P. & Wu, Q. Chemical weathering in Luzon, Philippines from clay mineralogy and major-element geochemistry of river sediments. *Appl. Geochem.* **24**, 2195–2205 (2009).
41. Liu, Z. et al. Climatic and tectonic controls on chemical weathering in tropical Southeast Asia (Malay Peninsula, Borneo, and Sumatra). *Chem. Geol.* **291**, 1–12 (2012).
42. Bayon, G. et al. Rare earth elements and neodymium isotopes in world river sediments revisited. *Geochim. Cosmochim. Acta* **170**, 17–38 (2015).
43. West, A. J. Thickness of the chemical weathering zone and implications for erosional and climatic drivers of weathering and for carbon-cycle feedbacks. *Geology* **40**, 811–814 (2012).
44. Zhao, Y. et al. Reconstruction of silicate weathering intensity and paleoenvironmental change during the late Quaternary in the Zhuoshui River catchment in Taiwan. *Quat. Int.* **452**, 43–53 (2017).
45. Hu, D. et al. Holocene evolution in weathering and erosion patterns in the Pearl River delta. *Geochem. Geophys. Geosyst.* **14**, 2349–2368 (2013).
46. Zhang, J. et al. History of Yellow River and Yangtze River delivering sediment to the Yellow Sea since 3.5 Ma: Tectonic or climate forcing? *Quat. Sci. Rev.* **216**, 74–88 (2019).
47. Skinner, L. C. et al. Rare Earth Elements in early-diagenetic foraminifer 'coatings': pore-water controls and potential palaeoceanographic applications. *Geochim. Cosmochim. Acta* **245**, 118–132 (2019).
48. Milliman, J. D., Farnsworth, K. L. *River Discharge to the Coastal Ocean: A Global Synthesis* (Cambridge University Press, 2013).
49. Jaques, A., Chappell, B. & Taylor, S. Geochemistry of cumulus peridotites and gabbros from the Marum Ophiolite Complex, northern Papua New Guinea. *Contrib. Mineral. Petrol.* **82**, 154–164 (1983).
50. Franke, W. A. The durability of rocks—developing a test of rock resistance to chemical weathering. *Am. J. Sci.* **309**, 711–730 (2009).
51. Pham, V. Q. et al. Dissolved rare earth elements distribution in the Solomon Sea. *Chem. Geol.* **524**, 11–36 (2019).
52. Wu, J., Liu, Z. & Zhou, C. Late quaternary glacial cycle and precessional period of clay mineral assemblages in the western pacific warm pool. *Chin. Sci. Bull.* **57**, 3748–3760 (2012).
53. Chamley, H. *Clay Sedimentology* (Springer, 1989).
54. Schopka, H., Derry, L. & Arcilla, C. Chemical weathering, river geochemistry and atmospheric carbon fluxes from volcanic and ultramafic regions on Luzon Island, the Philippines. *Geochim. Cosmochim. Acta* **75**, 978–1002 (2011).
55. Gaillardet, J., Dupré, B., Louvat, P. & Allègre, C. J. Global silicate weathering and CO_2 consumption rates deduced from the chemistry of large rivers. *Chem. Geol.* **159**, 3–30 (1999).
56. Liu, J. et al. Staged fine-grained sediment supply from the Himalayas to the Bengal Fan in response to climate change over the past 50,000 years. *Quat. Sci. Rev.* **212**, 164–177 (2019).
57. Kissel, C. et al. Monsoon variability and deep oceanic circulation in the western equatorial Pacific over the last climatic cycle: Insights from sedimentary magnetic properties and sortable silt. *Paleoceanography* **25**, PA3215 (2010).
58. Aldrian, E. & Susanto, R. Identification of three dominant rainfall regions within Indonesia and their relationship to sea surface temperature. *Int. J. Climatol.* **23**, 1435–1452 (2003).
59. DiNezio, P. N. et al. Glacial changes in tropical climate amplified by the Indian Ocean. *Sci. Adv.* **4**, eaat9658 (2018).

60. DiNezio, P. N. & Tierney, J. E. The effect of sea level on glacial Indo-Pacific climate. *Nat. Geosci.* **6**, 485–491 (2013).
61. Wan, S., Tian, J., Steinke, S., Li, A. & Li, T. Evolution and variability of the East Asian summer monsoon during the Pliocene: evidence from clay mineral records of the South China Sea. *Palaeogeogr. Palaeoclimatol. Palaeoecol.* **293**, 237–247 (2010).
62. Chen, Q., Liu, Z. & Kissel, C. Clay mineralogical and geochemical proxies of the East Asian summer monsoon evolution in the South China Sea during Late Quaternary. *Sci. Rep.* **7**, 42083 (2017).
63. Yu, Z., Colin, C., Bassinot, F., Wan, S. & Bayon, G. Climate-driven weathering shifts between highlands and floodplains. *Geochem. Geophys. Geosyst.* **21**, e2020GC008936 (2020).
64. Colin, C., Turpin, L., Bertaux, J., Desprairies, A. & Kissel, C. Erosional history of the Himalayan and Burman ranges during the last two glacial–interglacial cycles. *Earth Planet. Sci. Lett.* **171**, 647–660 (1999).
65. Beck, J. W. et al. A 550,000-year record of East Asian monsoon rainfall from 10Be in loess. *Science* **360**, 877–881 (2018).
66. Laskar, J. et al. A long-term numerical solution for the insolation quantities of the Earth. *Astron. Astrophys.* **428**, 261–285 (2004).
67. Lee, S.-S., Seo, Y.-W., Ha, K.-J. & Jhun, J.-G. Impact of the western North Pacific subtropical high on the East Asian monsoon precipitation and the Indian Ocean precipitation in the boreal summertime. *Asia-Pac. J. Atmos. Sci.* **49**, 171–182 (2013).
68. Diaz, H. F., Bradley, R. S. *The Hadley Circulation: Present, Past and Future* 1–5 (Springer, 2004).
69. Walczak, M. H. et al. Phasing of millennial-scale climate variability in the Pacific and Atlantic Oceans. *Science* **370**, 716–720 (2020).
70. Wu, Q. et al. Foraminiferal εNd in the deep north-western subtropical Pacific Ocean: tracing changes in weathering input over the last 30,000 years. *Chem. Geol.* **470**, 55–66 (2017).
71. Jian, Z. et al. Half-precessional cycle of thermocline temperature in the western equatorial Pacific and its bihemispheric dynamics. *Proc. Natl Acad. Sci.* **117**, 7044–7051 (2020).
72. Lisiecki, L. & Raymo, M. A Pliocene-Pleistocene stack of 57 globally distributed benthic $\delta^{18}O$ records. *Paleoceanography* **20**, PA1003 (2005).
73. Wan, S. et al. History of Asian eolian input to the West Philippine Sea over the last one million years. *Palaeogeogr. Palaeoclimatol. Palaeoecol.* **326**, 152–159 (2012).
74. Yu, Z. et al. Co-evolution of monsoonal precipitation in East Asia and the tropical Pacific ENSO system since 2.36 Ma: new insights from high-resolution clay mineral records in the West Philippine Sea. *Earth Planet. Sci. Lett.* **446**, 45–55 (2016).
75. Wan, S. et al. Human impact overwhelms long-term climate control of weathering and erosion in southwest China. *Geology* **43**, 439–442 (2015).
76. Cao, F. et al. Using lithium isotopes to quantitatively decode continental weathering signal: a case study in the Changjiang (Yangtze River) Estuary. *Sci. China Earth Sci.* **64**, 1698–1708 (2021).
77. Berger, A. & Loutre, M. F. Insolation values for the climate of the last 10 million years. *Quat. Sci. Rev.* **10**, 297–317 (1991).
78. Willeit, M., Ganopolski, A., Calov, R. & Brovkin, V. Mid-Pleistocene transition in glacial cycles explained by declining CO2 and regolith removal. *Sci. Adv.* **5**, eaav7337 (2019).
79. Luthi, D. et al. High-resolution carbon dioxide concentration record 650,000–800,000 years before present. *Nature* **453**, 379–382 (2008).
80. Friedrich, T., Timmermann, A., Tigchelaar, M., Elison Timm, O. & Ganopolski, A. Nonlinear climate sensitivity and its implications for future greenhouse warming. *Sci. Adv.* **2**, e1501923 (2016).
81. Friedrich, T., Timmermann, A. Using Late Pleistocene sea surface temperature reconstructions to constrain future greenhouse warming. *Earth Planet. Sci. Lett*. **530** https://doi.org/10.1016/j.epsl.2019.115911 (2020)
82. Meehl, G. A. et al. Context for interpreting equilibrium climate sensitivity and transient climate response from the CMIP6 Earth system models. *Sci. Adv.* **6**, eaba1981 (2020).
83. Timmermann, A. et al. Modeling obliquity and CO_2 effects on southern hemisphere climate during the past 408 ka.*J. Clim.* **27**, 186–1875 (2014).
84. Dang, H., Jian, Z., Kissel, C. & Bassinot, F. Precessional changes in the western equatorial Pacific Hydroclimate: a 240 kyr marine record from the Halmahera Sea, East Indonesia. *Geochem. Geophys. Geosyst.* **16**, 148–164 (2015).
85. Wei, E. A. & Driscoll, N. W. Clay mineralogy of Gulf of Papua Shelf and Pandora Trough deposits constrain sediment routing during the last sea-level cycle. *Sedimentology* **67**, 2502–2528 (2020).
86. Howell, A. L. et al. Fine sediment mineralogy as a tracer of Latest Quaternary sediment delivery to a dynamic continental margin: Pandora Trough, Gulf of Papua, Papua New Guinea. *Mar. Geol.* **357**, 108–122 (2014).
87. Rudnick, R., Gao, S., Holland, H. & Turekian, K. Composition of the continental crust. *Crust* **3**, 1–64 (2003).
88. Nesbitt, H. & Young, G. Early Proterozoic climates and plate motions inferred from major element chemistry of lutites. *Nature* **299**, 715–717 (1982).
89. Spratt, R. M. & Lisiecki, L. E. A Late Pleistocene sea level stack. *Climate* **12**, 1079–1092 (2016).

Acknowledgements

This study was supported by the Strategic Priority Research Program of Chinese Academy of Sciences (XDB42010402), the National Natural Science Foundation of China (42376055, 91958107, and 42176034), the Natural Science Foundation of Shandong (ZR2022YQ33), Youth Innovation Promotion Association, CAS (2020210), Laboratory for Marine Geology, Qingdao Pilot National Laboratory for Marine Science and Technology (MGQNLM-TD201902), and the National Key Research and Development Program of China (2022YFF0800503). D.J.W. is supported by a NERC independent research fellowship (NE/T011440/1). J.R. and K.-S.Y. receive funding from the Institute for Basic Science IBS-R028-D1 and IBS-R028-Y3. We thank Xuebo Yin for assistance with elemental chemistry measurements, and Delia Oppo and Hai Cheng for helpful discussions. We also thank three anonymous reviewers for their valuable comments that helped us to improve the manuscript.

Author contributions

Z.Y. and C.C. designed the study. X.T. and Z.Y. generated and analysed the geochemical data. Z.Y. wrote the original manuscript draft. C.C., D.J.W., and H.D. edited the original manuscript draft. J.R. and K.-S.Y. analysed the CESM1.2 simulations, made Fig. 5, and edited the manuscript. H.D. and P.D. contributed to the discussion section. H.D. and X.P. contributed to the age model. All authors read and edited the paper.

Competing interests

The authors declare no competing interests.

Additional information

Supplementary information The online version contains supplementary material available at https://doi.org/10.1038/s41612-024-00642-0.

Correspondence and requests for materials should be addressed to Zhaojie Yu or Jiaoyang Ruan.

Reprints and permissions information is available at http://www.nature.com/reprints

Publisher's note Springer Nature remains neutral with regard to jurisdictional claims in published maps and institutional affiliations.

Open Access This article is licensed under a Creative Commons Attribution 4.0 International License, which permits use, sharing, adaptation, distribution and reproduction in any medium or format, as long as you give appropriate credit to the original author(s) and the source, provide a link to the Creative Commons licence, and indicate if changes were made. The images or other third party material in this article are included in the article's Creative Commons licence, unless indicated otherwise in a credit line to the material. If material is not included in the article's Creative Commons licence and your intended use is not permitted by statutory regulation or exceeds the permitted use, you will need to obtain permission directly from the copyright holder. To view a copy of this licence, visit http://creativecommons.org/licenses/by/4.0/.

© The Author(s) 2024

Supporting Material for

Late Pleistocene island weathering and precipitation in the Western Pacific Warm Pool

This PDF file includes:

Supplementary Information

Fig. S1 to S9

Supplementary Information

Regional climatic setting

A detailed overview of the different precipitation regimes found in the modern Indo-Pacific region was presented in our previous study [1]. Briefly, three climatic regions can be identified in the Indo-Pacific region based on monthly rainfall data from meteorological stations spanning 1961-1993 in the Global Historical Climatology Network (GHCN) database [2] (Fig. S1). The potential source area supplying sediments to MD01-2385 (northwestern part of New Guinea) is mostly located in region C, with higher precipitation in boreal summer, and lower precipitation in boreal winter [2] (Fig. S1). The rest of New Guinea island, however, is in region A, with the opposite rainfall seasonality: higher precipitation in austral summer, and lower precipitation in austral winter (Fig. S1). Meanwhile, region B shows biannual precipitation peaks in October–November and March–May, which are probably induced by the migration of the ITCZ [2]. In the western part (Indian Ocean), there is a relatively simple boundary between region A to the south and region B to the north. In contrast, in the eastern part (Pacific Ocean), region C displays a complex intrusion pattern, with areas to both the west and the east belonging to region A (Fig. S1). This distribution may arise from the westwards flow of the Indonesian Throughflow that transports warm water from the Pacific warm pool, thereby generating an atmospheric convection centre and bringing precipitation to the region during boreal summer, while the opposite scenario occurs during boreal winter [2]. Additionally, the monthly precipitation anomaly over the source area of MD01-2385 is highly correlated with the Southern Oscillation Index, and Niño 3.4 sea-surface temperature anomalies [1].

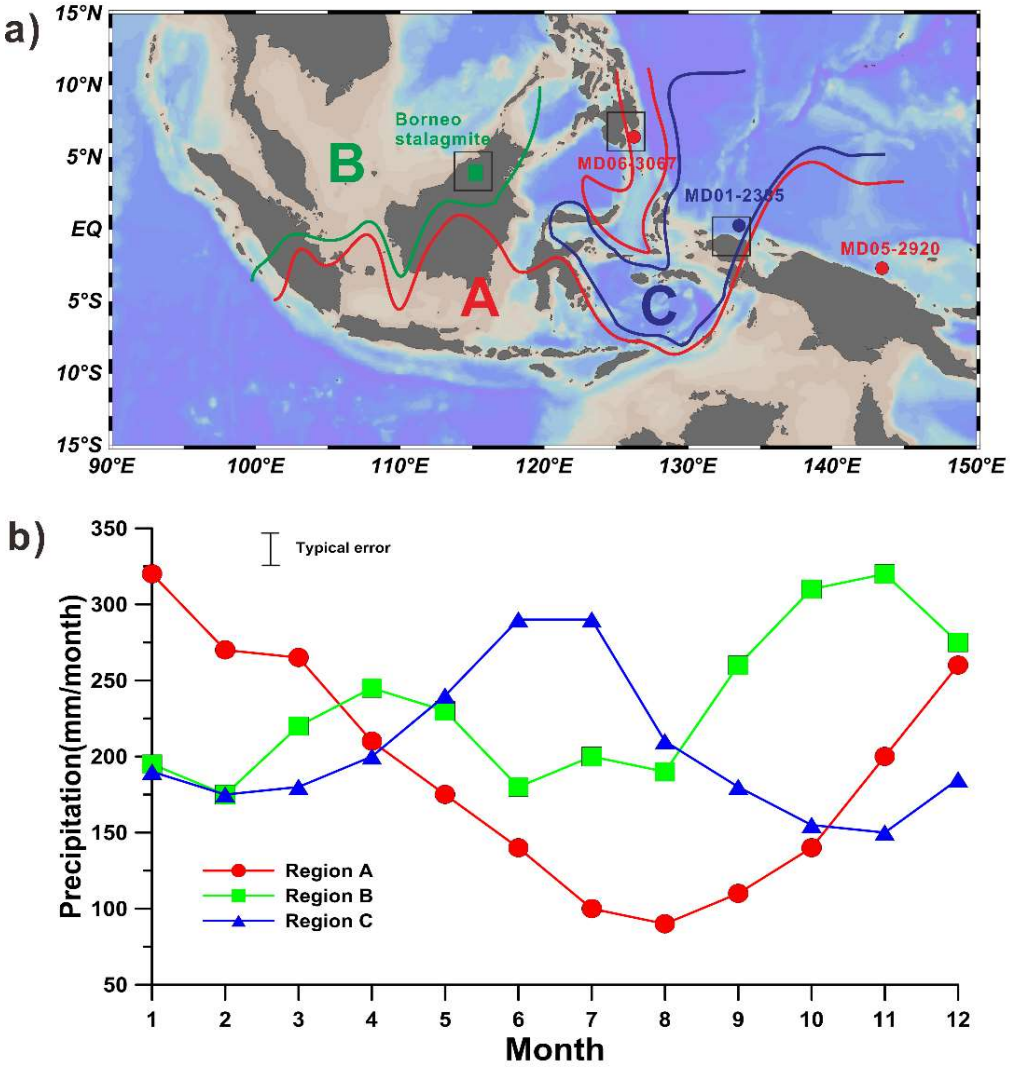

Fig. S1 Modern rainfall patterns in the Indo-Pacific region. (a) Distribution of hydrological regions A to C, based on the modern observed monthly mean rainfall patterns from the Global Historical Climatology Network (GHCN) database [2]. Locations of representative late Quaternary hydroclimate reconstructions from each region are given by dots in the same colour: MD05-2920 [3] and MD06-3067 [4] from region A (red line); Borneo stalagmite [5-7] from region B (green line); and MD01-2385 (this study) from region C (blue line). Note that region A is split into two parts by region C. The three black boxes represent the location of the simulated precipitation data used for comparison to those records (3.75° x 3.75°) [8-10]*8-10*. (b) Modern rainfall patterns in regions A (maximum in December-January), B (maximum in October-November), and C (maximum in June-July). Typical error estimate is also shown. Figure modified from *Aldrian and Susanto* [2].

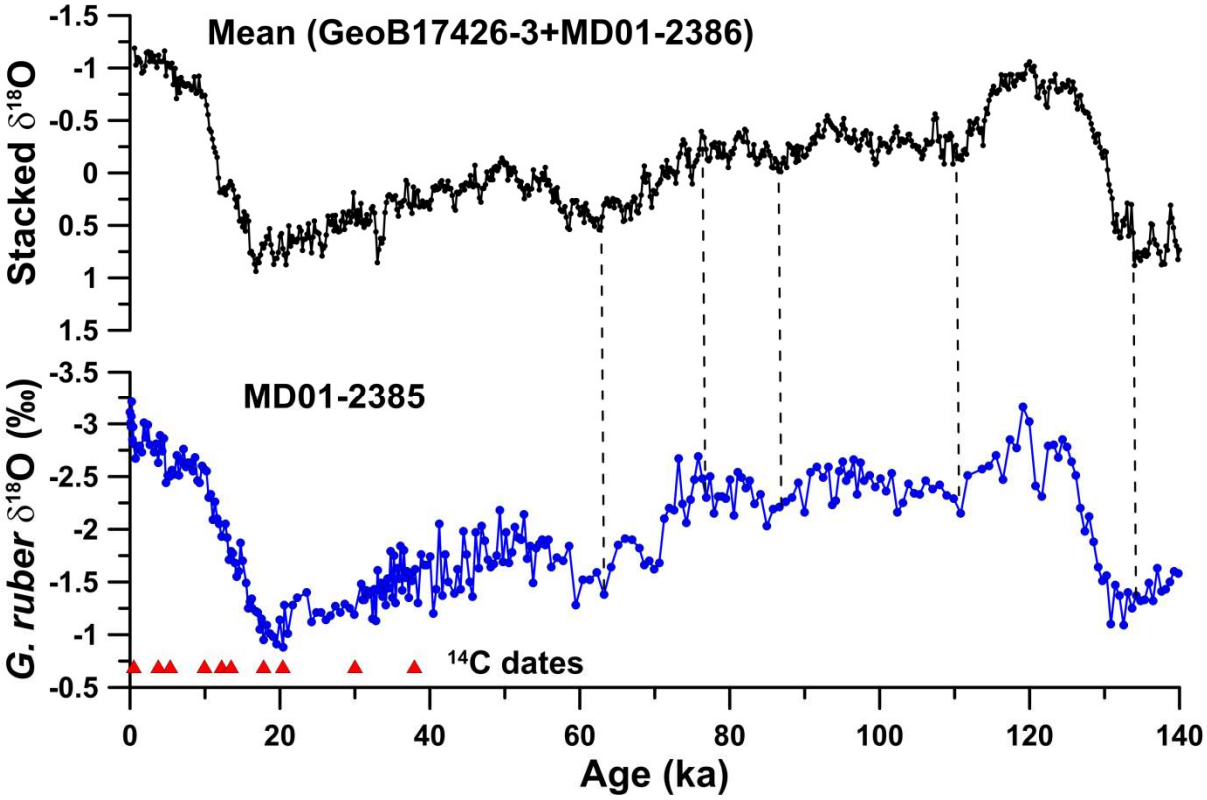

Fig. S2 Planktonic foraminiferal $\delta^{18}O$ record and age model for core MD01-2385 since 140 ka[11]. The age model from 0-40 ka is based on radiocarbon dates [1,12] (red triangles along axis). From 40-140 ka, the age model is based on tuning of the planktonic foraminifera *G. ruber* $\delta^{18}O$ record from core MD01-2385 to the stacked *G. ruber* $\delta^{18}O$ record from nearby cores GeoB17426-3 [13] and MD01-2386 [14] (tie points shown by black dashed lines; see Fig. 1b for the core locations). The age models of the latter cores were established by tuning of their benthic foraminiferal $\delta^{18}O$ records to the LR04 benthic $\delta^{18}O$ stack [15].

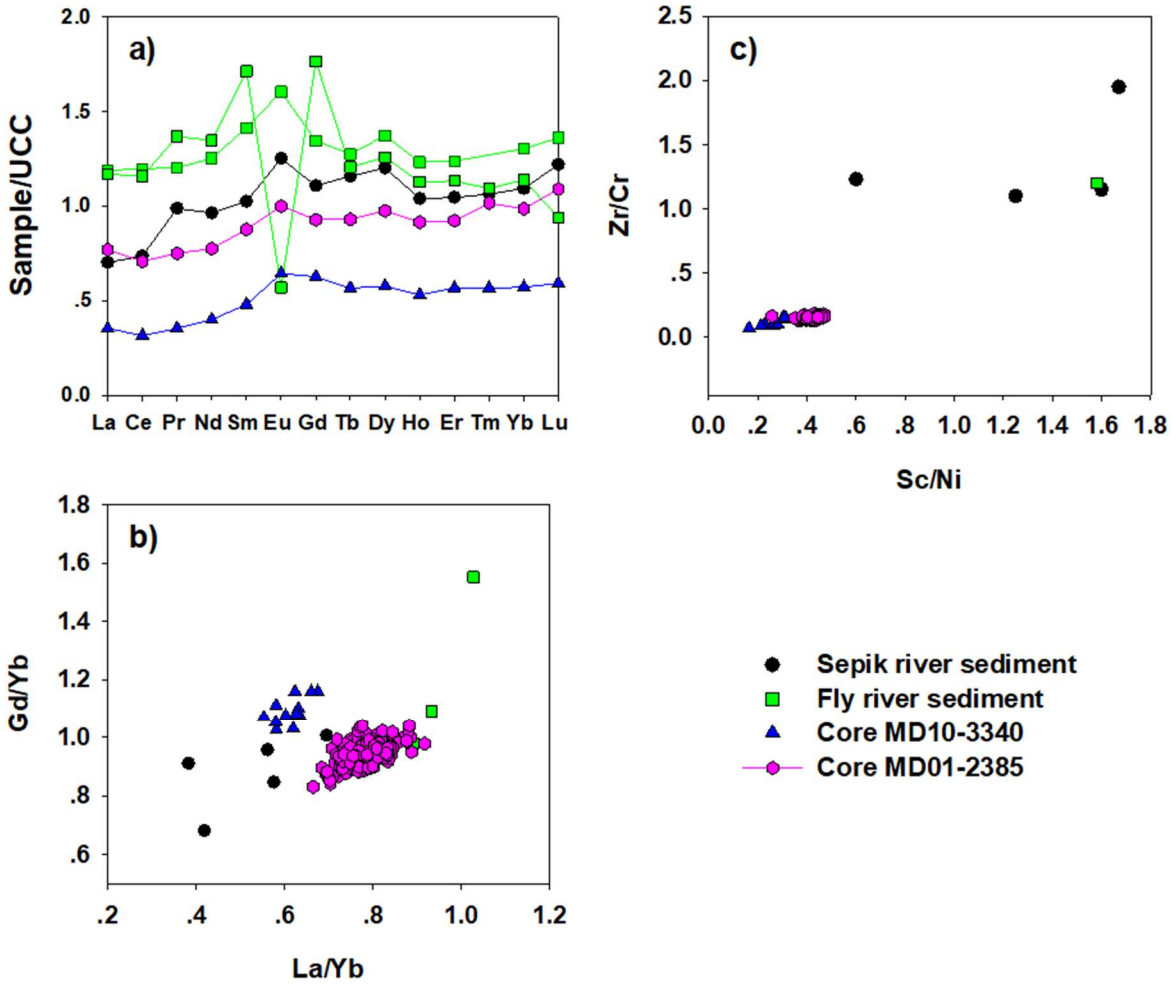

51

52 **Fig. S3** (a) Average sediment REE patterns normalised to the Upper Continental Crust (UCC)
53 [16] for Sepik river [17], Fly river [17,18], core MD10-3340 [19], and core MD01-2385 (this study). (b)
54 UCC normalised Gd/Yb versus La/Yb in those sediments [16,20]. (c) Zr/Cr versus Sc/Ni in those
55 sediments. These plots indicate that the sediments in core MD01-2385 are mostly supplied by
56 local sources in northwest New Guinea via small mountainous rivers, while a significant
57 influence from the Sepik or Fly rivers can be excluded based on their different REE patterns
58 and/or elemental ratios.

59

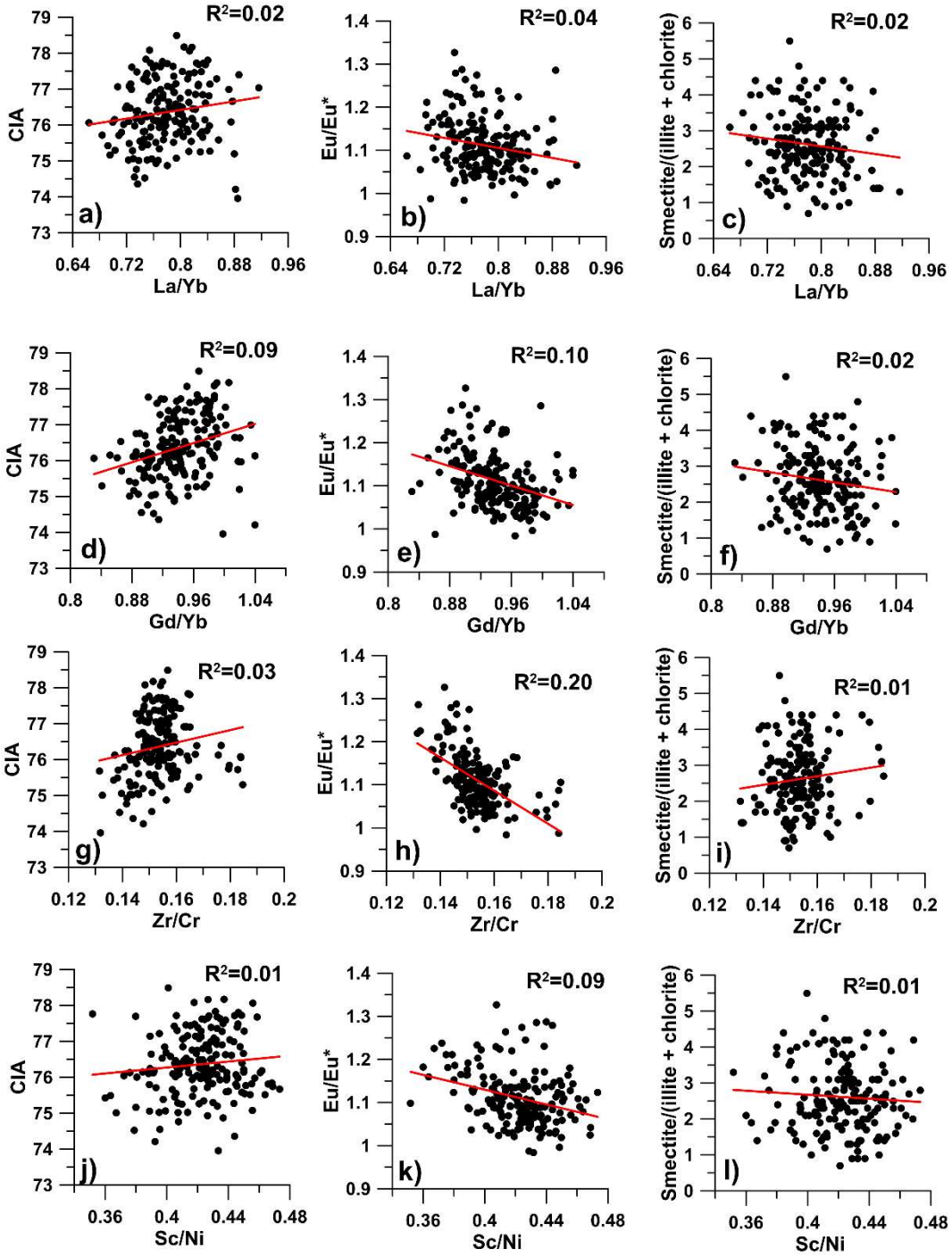

60

61 **Fig. S4** Cross plots of provenance indicators (La/Yb, Gd/Yb, Zr/Cr, and Sc/Ni) with
62 weathering and erosion proxies (CIA, Eu/Eu*, and smectite/(illite+chlorite) ratios) in core
63 MD01-2385. La/Yb and Gd/Yb are UCC-normalised data [16,20]. The lack of obvious
64 correlations implies that there is an insignificant effect of sediment source changes on the
65 weathering and erosion proxies.

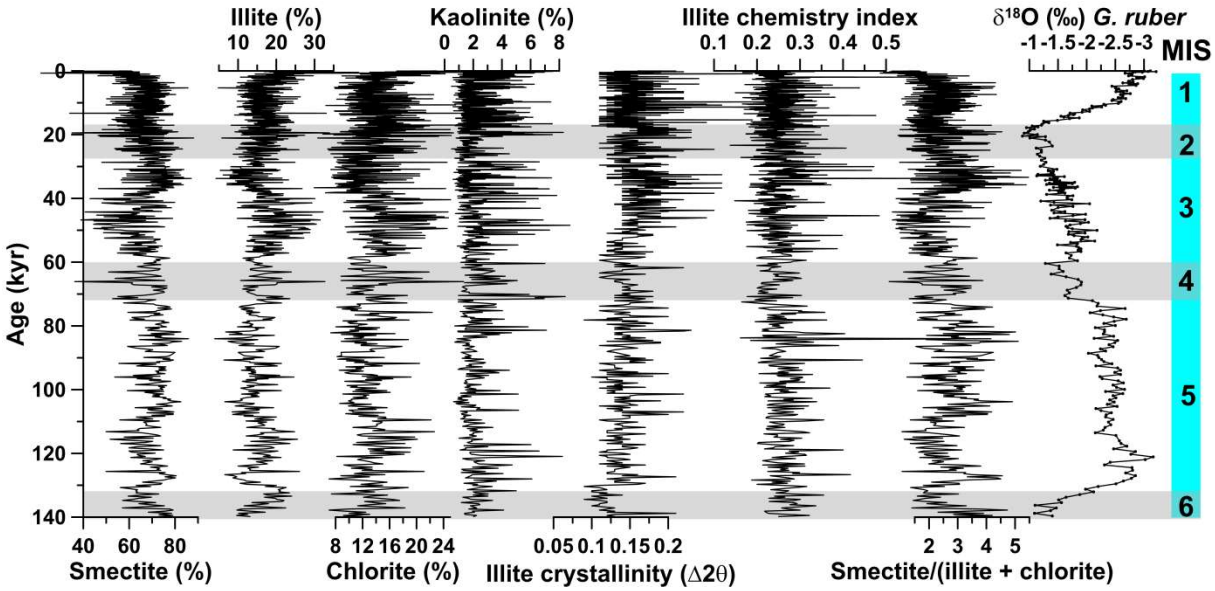

Fig. S5 Downcore records of clay mineralogy in core MD01-2385. Also shown are the planktonic foraminifera G. *ruber* $\delta^{18}O$ record from core MD01-2385 (this study) and the timing of marine isotope stages (MIS) 1 to 6. Grey shaded bars indicate glacial periods (MIS 2, 4, and 6).

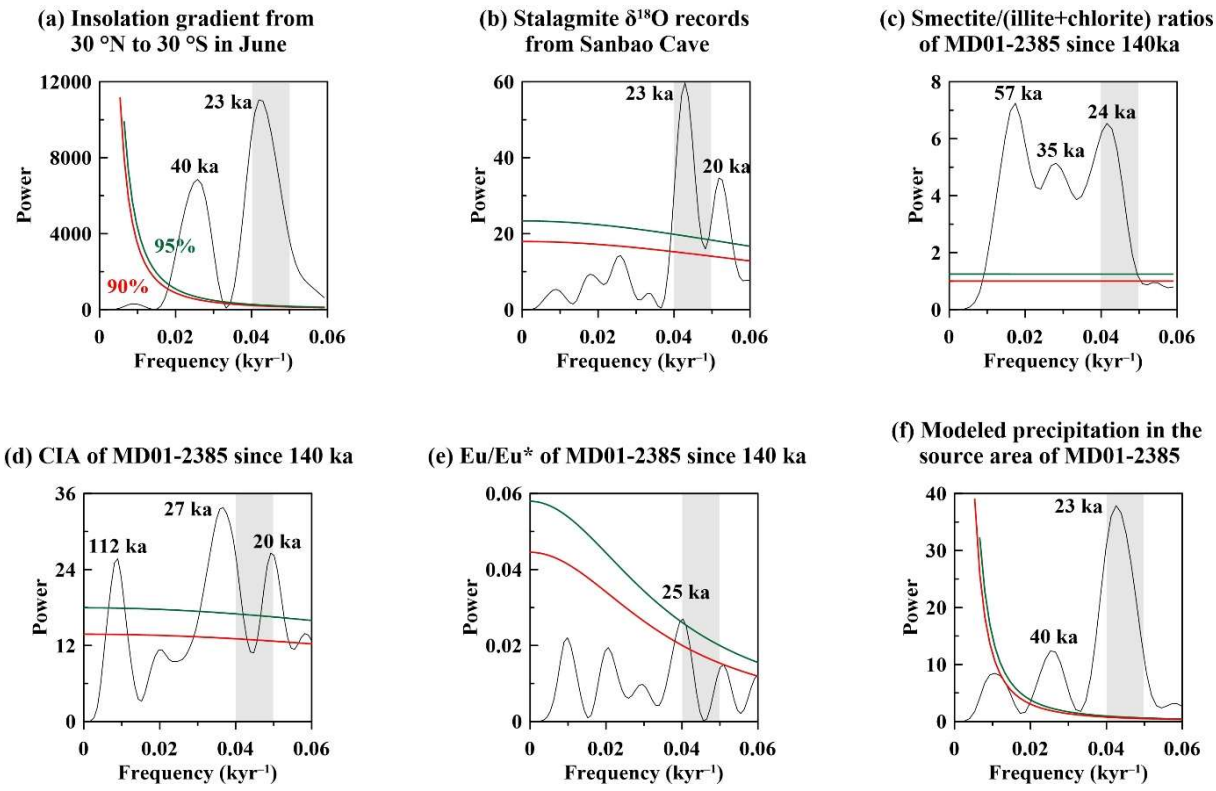

Fig. S6 Spectral analysis of (a) insolation gradient from 30 °N to 30 °S in June [21], (b) stalagmite $\delta^{18}O$ records from Sanbao Cave [22], (c) smectite/(illite+chlorite) ratios in core MD01-2385 since 140 ka (this study), (d) CIA in core MD01-2385 since 140 ka (this study), (e) Eu/Eu* in core MD01-2385 since 140 ka (this study), and (f) modelled precipitation in the source area of MD01-2385 [8-10]. The spectral analysis was performed with PAST software; the window function is rectangle; the oversample is 8; the segment is 2 for (a), (c), and (f), and is 1 for (b), (d), and (e). The 95% and 90% confidence curves are represented by green and red lines, respectively. The grey bars indicate a periodicity of 20-25 kyr.

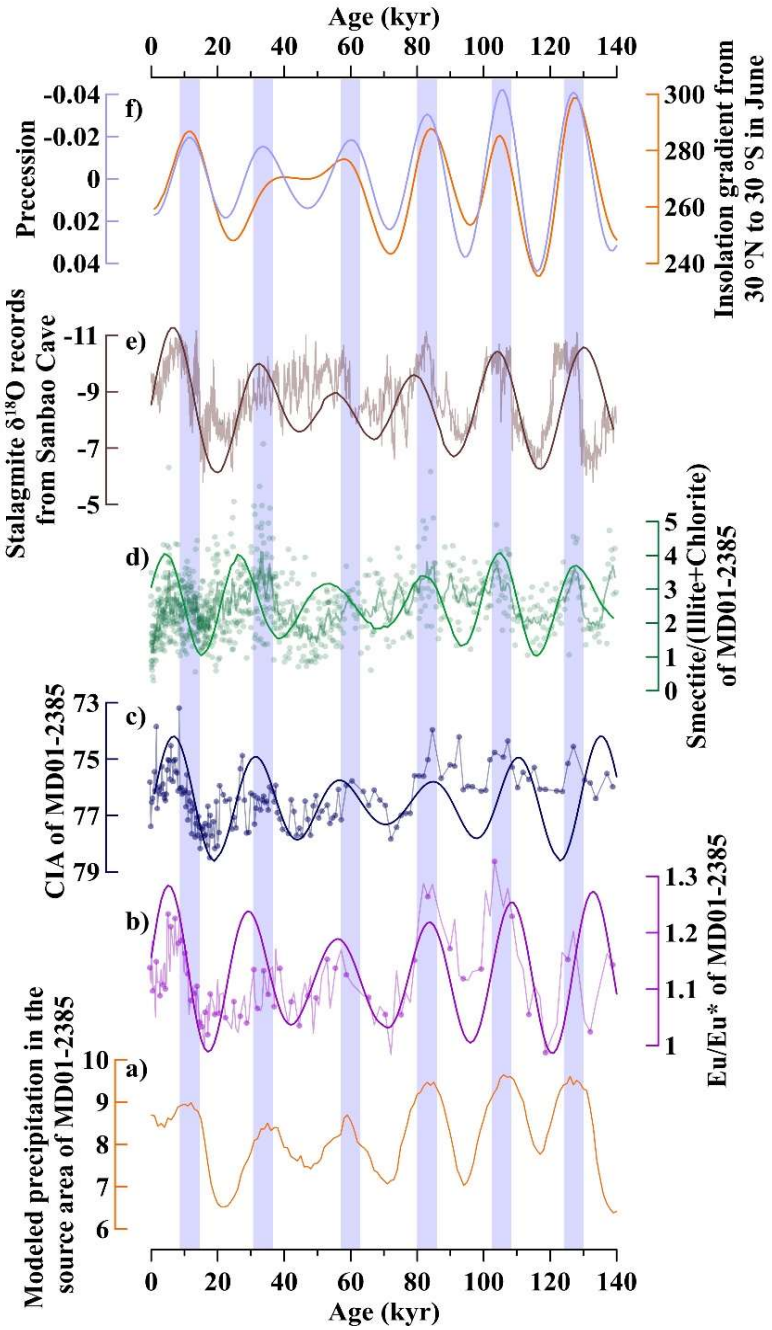

Fig. S7 Similar precession-dominated cycles in (a) modelled precipitation in the source area of core MD01-2385, (b) Eu/Eu* in core MD01-2385, (c) CIA in core MD01-2385, (d) smectite/(illite+chlorite) in core, (e) stalagmite $\delta^{18}O$ records from Sanbao Cave [22], and (f) north-south insolation gradient (orange) and precession (purple) [21]. The pale points and lines in (b-e) represent the raw data. The superimposed curves are precessional band-pass filtered data (b-e), filtered by PAST with a central frequency of 0.043 kyr^{-1} and a bandwidth of 0.01 kyr^{-1}. The light purple shaded bars represent the precession minima.

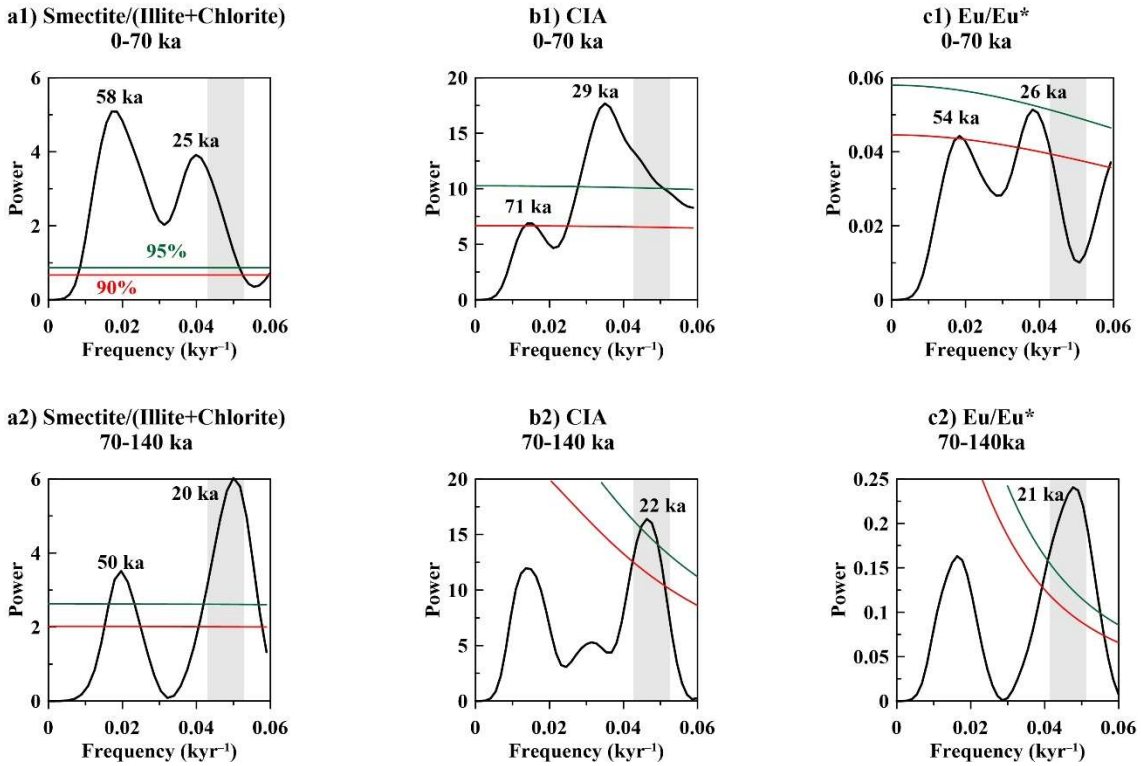

Fig. S8 Spectral analysis of weathering records: (a) smectite/(illite+chlorite); (b) CIA; (c) Eu/Eu* in core MD01-2385 between the period 0-70 ka (upper, labelled 1) and 70-140 ka (lower, labelled 2). The spectral analysis was performed with PAST software with a rectangle window function; the oversample is 10; the segment is 1. The 95% and 90% confidence curves are represented by green and red lines, respectively. The grey bars indicate a periodicity of 19-23 kyr.

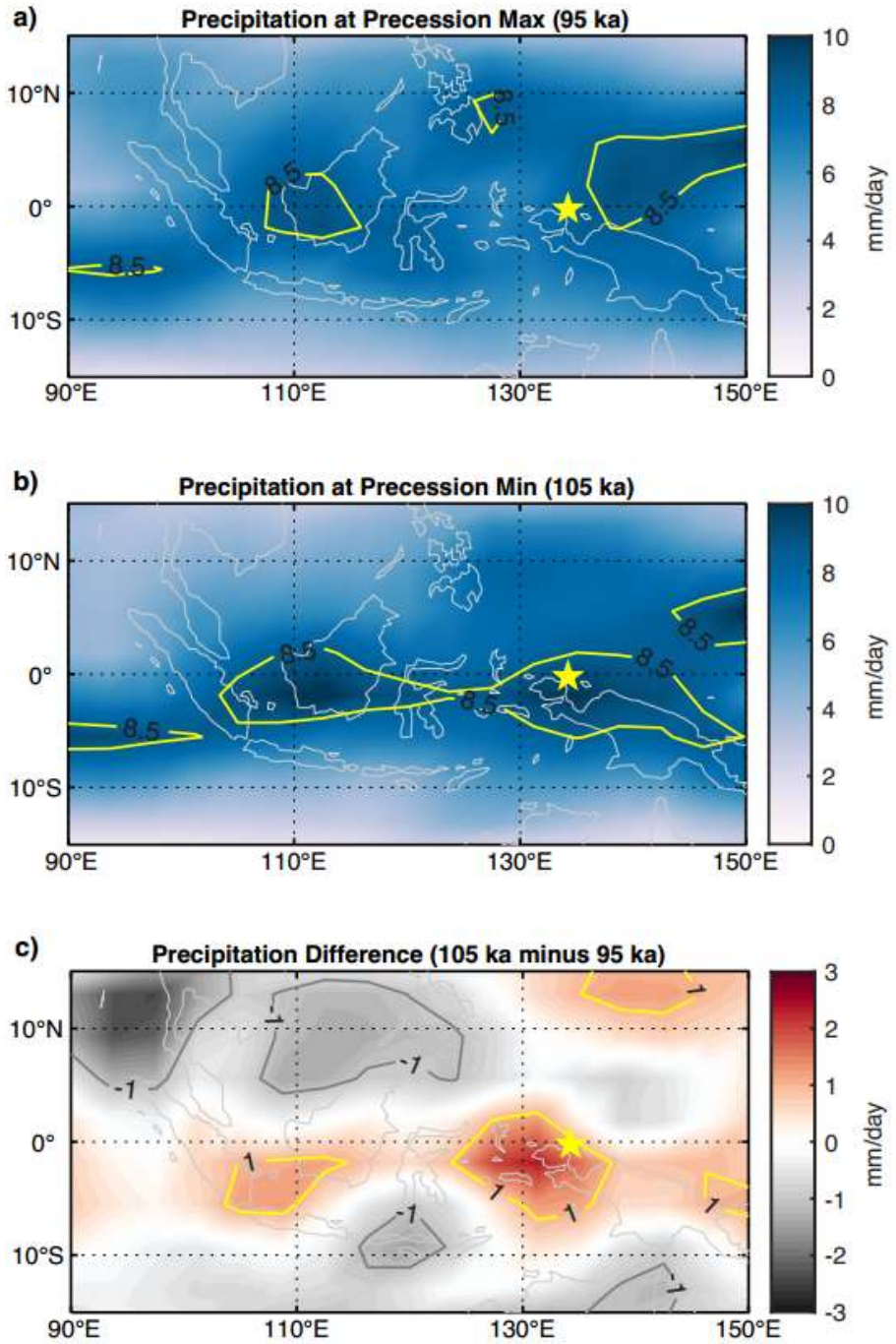

101
102

103 **Fig. S9** Precipitation over the Indo-Pacific region simulated by CESM during (a) precession
104 maximum (95 ka), (b) precession minimum (105 ka), and (c) their difference (105 ka minus
105 95 ka) [8-10]. See also Fig. 5 in the main text.

106
107
108
109

References

1 Yu, Z. *et al.* Millennial-scale precipitation variability in the Indo-Pacific region over the last 40 kyr. *Geophysical Research Letters* **n/a**, e2022GL101646 (2023). https://doi.org/https://doi.org/10.1029/2022GL101646

2 Aldrian, E. & Susanto, R. Identification of three dominant rainfall regions within Indonesia and their relationship to sea surface temperature. *International Journal of Climatology: A Journal of the Royal Meteorological Society* **23**, 1435-1452 (2003).

3 Tachikawa, K. *et al.* The precession phase of hydrological variability in the Western Pacific Warm Pool during the past 400 ka. *Quaternary Science Reviews* **30**, 3716-3727 (2011). https://doi.org/https://doi.org/10.1016/j.quascirev.2011.09.016

4 Kissel, C. *et al.* Monsoon variability and deep oceanic circulation in the western equatorial Pacific over the last climatic cycle: Insights from sedimentary magnetic properties and sortable silt. *Paleoceanography* **25** (2010).

5 Carolin, S. A. *et al.* Northern Borneo stalagmite records reveal West Pacific hydroclimate across MIS 5 and 6. *Earth and Planetary Science Letters* **439**, 182-193 (2016). https://doi.org/https://doi.org/10.1016/j.epsl.2016.01.028

6 Carolin, S. A. *et al.* Varied response of western Pacific hydrology to climate forcings over the last glacial period. *Science* **340**, 1564-1566 (2013).

7 Partin, J. W., Cobb, K. M., Adkins, J. F., Clark, B. & Fernandez, D. P. Millennial-scale trends in west Pacific warm pool hydrology since the Last Glacial Maximum. *Nature* **449**, 452-455 (2007).

8 Ruan, J. *et al.* Climate shifts orchestrated hominin interbreeding events across Eurasia. *Science* **381**, 699-704 (2023). https://doi.org/10.1126/science.add4459

9 Timmermann, A. *et al.* Climate effects on archaic human habitats and species successions. *Nature* **604**, 495-501 (2022). https://doi.org/10.1038/s41586-022-04600-9

10 Yun, K.-S. *et al.* A transient coupled general circulation model (CGCM) simulation of the past 3 million years. *Clim. Past* **19**, 1951-1974 (2023). https://doi.org/10.5194/cp-19-1951-2023

11 Tang, X. *et al.* Orbital hydroclimate variability revealed by grain-size evidence in the tropical Pacific Islands since 140 ka. *Global and Planetary Change*, 104429 (2024). https://doi.org/https://doi.org/10.1016/j.gloplacha.2024.104429

12 Wu, Q. *et al.* Foraminiferal εNd in the deep north-western subtropical Pacific Ocean: Tracing changes in weathering input over the last 30,000years. *Chemical Geology* **470**, 55-66 (2017). https://doi.org/https://doi.org/10.1016/j.chemgeo.2017.08.022

13 Hollstein, M. *et al.* The impact of astronomical forcing on surface and thermocline variability within the Western Pacific Warm Pool over the past 160 kyr. *Paleoceanography and Paleoclimatology* **35**, e2019PA003832 (2020).

14 Jian, Z. *et al.* Half-precessional cycle of thermocline temperature in the western equatorial Pacific and its bihemispheric dynamics. *Proceedings of the National Academy of Sciences* **117**, 7044-7051 (2020).

15 Lisiecki, L. & Raymo, M. A Pliocene-Pleistocene stack of 57 globally distributed benthic $\delta^{18}O$ records. *Paleoceanography* **20, PA1003** (2005).

16 Rudnick, R., Gao, S., Holland, H. & Turekian, K. Composition of the continental crust. *The crust* **3**, 1-64 (2003).

17 Hannigan, R. E. & Sholkovitz, E. R. The development of middle rare earth element enrichments in freshwaters: weathering of phosphate minerals. *Chemical Geology* **175**, 495-508 (2001). https://doi.org/https://doi.org/10.1016/S0009-2541(00)00355-7

18 Bayon, G. *et al.* Rare earth elements and neodymium isotopes in world river sediments revisited. *Geochimica et Cosmochimica Acta* **170**, 17-38 (2015).
19 Dang, H., Jian, Z., Kissel, C. & Bassinot, F. Precessional changes in the western equatorial Pacific Hydroclimate: A 240 kyr marine record from the Halmahera Sea, East Indonesia. *Geochemistry, Geophysics, Geosystems* **16**, 148-164 (2015).
20 Evensen, N. M., Hamilton, P. & O'nions, R. Rare-earth abundances in chondritic meteorites. *Geochimica et cosmochimica Acta* **42**, 1199-1212 (1978).
21 Laskar, J. *et al.* A long-term numerical solution for the insolation quantities of the Earth. *Astronomy & Astrophysics* **428**, 261-285 (2004).
22 Cheng, H. *et al.* The Asian monsoon over the past 640,000 years and ice age terminations. *Nature* **534**, 640-646 (2016).